Schweizerische Eidgenossenschaft
Confédération suisse
Confederazione Svizzera
Confederaziun svizra

Department of the Environment,
Transport, Energy and Communication DETEC

**Swiss Federal Office of Energy SFOE**
Energy Research

**Final report**

# Development and experimental validation of a two-phase flow fluidized bed model for energy conversion processes, with application to biogas methanation

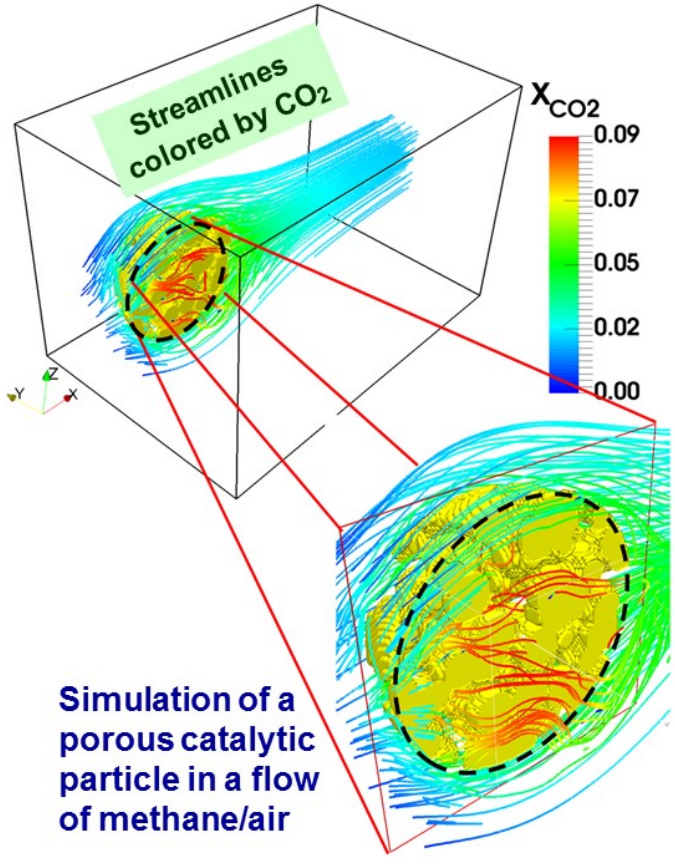


**Date:** 06 02 2019

**Place:** Bern

**Publisher:**
Swiss Federal Office of Energy SFOE
Research Programme XY
CH-3003 Bern
www.bfe.admin.ch
energieforschung@bfe.admin.ch

**Co-financed by:**
-

**Agent:**
Paul Scherrer Institute
CH-5232, Villigen PSI
www.psi.ch

**Author:**
Ioannis Mantzaras, ioannis.mantzaras@psi.ch
Amin Safi: amin.safi@psi.ch

**SFOE head of domain:** Dr. Carina Alles, Carina.Alles@bfe.admin.ch

**SFOE programme manager:** Dr. Carina Alles, Carina.Alles@bfe.admin.ch
**SFOE contract number:** SI/501490-01

# Summary

There is nowadays a sustained effort to convert biomass feedstock into biogas (a mixture comprising mostly CO and $H_2$) and then to convert biogas into synthetic natural gas (SNG) in dedicated methanation fluidized beds (FBs). Bio-based SNG is a clean fuel and and can be used in the existing gas distribution infrastructure. Advancing the knowledge of the physicochemical processes in methanation FBs is of prime importance for process optimization and hence for the secure production of sustainable fuels. Experimental studies in laboratory-scale FBs at Paul Scherrer Institute have fostered the understanding of the methanation catalytic kinetics and have assessed the impact of operating conditions on biogas conversion and methane production. In these studies, the solid phase comprises catalytic $Ni/Al_2O_3$ particles. Besides the experiments, 1-D models have been applied at PSI to simulate methanation FBs. However, little has been done to assess the impact of the particle's internal porosity on the reaction and diffusion processes at the particle level. As the total intra-particle porosity amounts to ~25% of the total FB void volume, models accurately describing the convection/diffusion/reaction processes in and around typical $Ni/Al_2O_3$ porous particles (sizes of 0.15-0.55 mm) are necessary.

The project has developed, by means of the lattice Boltzmann (LB) methodology for the flow field and a Lagrangian particle tracking method, a numerical code that predicts the chemical composition of the gas trapped inside $Ni/Al_2O_3$ particles having realistic porous networks. The porous network of representative $Ni/Al_2O_3$ catalytic particles has been assessed by phase-contrasted X-ray tomography measurements at the Swiss Light Source (SLS) of PSI. The developed numerical model allows for particle movement in domains of gaseous flows comprising a few millimeters in each direction. Three-dimensional transient simulations have been applied to benchmark the convection, diffusion, and catalytic reaction of various chemical species around each catalytic particle as well as within its internal micro-pore structure. The built model can be used to assess the impact of the fluidized bed operating conditions, catalytic particle characteristics (size and porosity) and catalytic reactivity on the resulting chemical composition differences between the intra-particle gas and the gas surrounding the catalytic particles. Apart from the simulation of biogas methanation catalytic particles, the developed code can also be used in other industrial applications such as polyethylene production, granulation FBs and fluid catalytic cracking (FCC).

# Zusammenfassung

Die Umwandlung von Biomasse in Biogas, ein Gasgemisch vorwiegend aus Kohlenmonoxid und Wasserstoff, welches anschliessend in speziellen Methanisierungs-Wirbelschichten zu Biomethan (SNG, Bio-SNG) weiterverarbeitet wird, gewinnt zunehmend an Bedeutung. SNG ist ein sauberer und CO2-neutraler Kraft- und Brennstoff, welcher in vorhandene Verteilinfrastrukturen eingespeist werden kann. Zur Sicherstellung der Produktion dieses nachhaltigen Energieträgers müssen die grundlegenden Prozesse in der katalytischen Wirbelschicht verstanden werden. Labormessungen am Paul Scherrer Institut haben das Verständnis der Kinetik der katalytischen Methanisierung gefestigt und den Einfluss der Betriebsbedingungen auf die Biomasseumsetzung und die Biomethanproduktion bestimmt. Bei diesen Laborexperimenten bestand die Festkörperkomponente aus katalytischen $Ni/Al_2O_3$-Partikeln in der Grössenordnung von 0.15 bis 0.55 mm. Parallel dazu wurde die Methanisierung mit 1-D-Modellen simuliert. Bis anhin wurde jedoch kaum etwas unternommen, um den Einfluss der inneren Porosität der Partikel auf die Reaktionen und die Diffusion auf Partikelebene zu bestimmen. Da die Porosität innerhalb der Partikel immerhin etwa 25% des Leervolumens der Wirbelschicht ausmacht, sind neue Modelle, die die Konvektion, die Diffusion und die Reaktionen innerhalb der Partikel und in unmittelbarer Nähe korrekt beschreiben, unabdingbar.

Im Rahmen des Projekts wurde ein Programm auf der Basis der Lattice-Boltzmann-Methode (LB) entwickelt, welches die chemische Zusammensetzung des Gases innerhalb eines $Ni/Al_2O_3$-Katalysator-partikels berechnet. Eine Röntgentomographie eines repräsentativen Katalysatorpartikels wurde an der Swiss Light Source (SLS) des PSI durchgeführt. Damit konnte im Programm eine realistische Struktur des Porennetzwerks innerhalb der Partikel verwendet werden. Die numerische Berechnung berücksichtigt mit einer Lagrange-Partikelverfolgung Bewegungen des Partikels im Gasraum im Bereich mehrerer Millimeter. Mit der Simulation dreidimensionaler Transienten wurden schliesslich die Konvektion, die Diffusion und die katalytischen Reaktionen verschiedener chemischer Komponenten an und im Partikel bewertet. Das erarbeitete Modell erkennt den Einfluss der Betriebsbedingungen der Wirbelschicht, der Partikelgrösse, der Porosität und der katalytischen Reaktivität auf die Differenzierung der Gaszusammensetzungen zwischen Gasraum und den Poren der Partikel. Dieser Code kann nicht nur für die Simulation für katalytischen Reaktionen von Partikeln verwendet werden. Er findet ebenso seine Anwendung in der Industrie. Zum Beispiel für die Polyethylen Produktion, Wirbelschichten für die Granulation und für «fluid catalytic cracking» (FCC).

# Résumé

Il y a aujourd'hui un effort soutenu pour convertir la matière première de biomasse en un biogaz (un mélange composé essentiellement de CO et $H_2$), puis pour convertir ce biogaz en gaz naturel synthétique (GNS) dans les lits fluidisés (LF) de méthanisation. Le GNS biologique est un combustible propre et peut être aisément utilisé dans les infrastructures de distribution de gaz existantes. Il est primordial de faire progresser les connaissances des processus physicochimiques dans les LF de méthanisation afin d'optimiser les procédés et ainsi produire de manière sécurisée des combustibles durables. Des études expérimentales dans les LF de laboratoire au Paul Scherrer Institute ont consolidé la compréhension de la cinétique de la méthanisation catalytique et ont évalué l'impact des conditions d'opérations sur la conversion de biogaz et la production de méthane. Dans ces études, la phase solide est constituée de particules catalytiques de $Ni/Al_2O_3$. De plus, des modèles 1-D ont été appliqués afin de simuler les LF de méthanisation au PSI. Cependant, peu d'efforts ont été consentis pour évaluer l'impact de la porosité interne de la particule sur les processus de réaction et de diffusion. Comme la porosité intra-particulaire représente jusqu'à ~25% du volume vide du LF, des modèles décrivant avec précision les processus de convection/diffusion/réaction à l'intérieur et autour des particules catalytiques typiques de $Ni/Al_2O_3$ (d'une taille de 0.15-0.55 mm) sont nécessaires.

Le projet a développé, au moyen de la méthode de lattice Boltzmann (LB) pour l'écoulement et d'un modèle de dépistage des particules Lagrangien, un code numérique prédisant la composition chimique du gaz piégé dans des particules de $Ni/Al_2O_3$ possédant un réseau poreux réaliste. Le réseau poreux des particules catalytiques $Ni/Al_2O_3$ représentatives a été analysé par tomographie avec des rayons X à contraste de phase au Swiss Light Source (SLS) du PSI. Le modèle numérique développé permet des déplacements de la particule dans un domaine d'écoulement gazeux de quelques millimètres d'épaisseur dans chaque direction. Des simulations transitoires tri-dimensionnelles ont été utilisées afin de vérifier les phénomènes de convection, diffusion et les réactions catalytiques de diverses espèces chimiques autour de chaque particule catalytique ainsi qu'à l'intérieur de sa structure microporeuse. Le modèle peut être utilisé pour évaluer l'impact des conditions d'opération du lit fluidisé, des caractéristiques des particules catalytiques (taille et porosité) ainsi que de la réactivité catalytique sur la différence de composition chimique résultante entre le gaz intra-particulaire et le gaz entourant les particules catalytiques. Le code, outre la simulation de particules catalytiques réactives, peut aussi être utilisé pour d'autres applications industrielles telles que les LFs utilisés pour la granulation, la production de polyéthylène et le craquage catalytique fluide (CCF).

Seite absichtlich frei

# Contents

# List of abbreviations

| | |
|---|---|
| AMR | Adaptive mesh refinement |
| FB | Fluidized bed |
| LB | Lattice Boltzmann |
| MCP | Multiple catalytic particles |
| RDPM | Resolved discrete particle model |
| SCP | Single catalytic particle |
| TFM | Two fluid model |
| XTM | X-ray tomography |

# 1 Introduction

Fluidized beds (FB) are two-phase flow mixtures of particulate solid material and fluid, which are used in numerous industrial systems for the efficient implementation of various physical and chemical processes. Fluidized beds have been widely used in technological processes such as cracking and reforming of hydrocarbon oils [1-2], polyethylene production, gasification of coal and biomass [3], Fisher Tropsch synthesis, granulation, nuclear fuel preparation, solid and waste combustion [4] and methanation of biogas derived synthesis gas [5-8]. The last process is of particular interest for Paul Scherrer Institute (PSI), whereby the Group of Thermo Chemical Engineering (Drs. S. Biollaz and T. Schildhauer) investigates the conversion of biomass feedstock to Synthetic Natural Gas (SNG) as a means to produce a clean and $CO_2$ neutral fuel [6-8].

The term “fluidized bed” refers to particular states of the solid/fluid mixture that exist between two limiting states —fluid percolation in the vertical direction through a fixed bed of particulate solids and the free fall of the particles through the stagnant fluid due to gravity. Common characteristic of all FB states in vertical flow (upward or downward flow of fluid, particles, or both) is the existence of a fluid-to-particle relative velocity and drag force. The fluidized state is established when a fixed bed of the particulate material is penetrated vertically with fluid at a sufficiently high velocity to break up the bed. When the critical velocity (minimum fluidization velocity) is reached, the solid particles start floating, moving chaotically and colliding. Mutual contacts between the particles are of short duration and the forces between them are weak. The particulate solid material is then in the fluidized state. The mean particle distance grows with increasing fluid velocity, causing the bed height to rise.

For gas velocities above the minimum fluidization velocity, voids, also referred to as bubbles, form and the FB can be treated as consisting of two phases: bubbles, inside which there are virtually no particles, and a particulate phase (emulsion or dense phase) which is in a condition similar to that of the bed at the minimum fluidization velocity. Bubbles forming at the bed bottom (distributor plate) rise up, grow and coalesce, producing bigger bubbles that in turn break up into smaller ones. This is illustrated in the simulation results of Figs. 1(a1, a2) (obtained by Verma et al. [9], using a two fluid model (TFM) discussed in the forthcoming Section 2.1.1), showing instantaneous three dimensional bubble distributions at PSI’s large methanation fluidized bed [8, 10]. Two configurations are shown: Fig. 1(a1) for a bed without tubes and Fig. 1(a2) for a bed with vertical cooling tubes [8]. On the bed surface (the irregular surface delineating the bed height, see Fig. 1(a1)), bubbles burst, ejecting particles far from it. This bubble behavior creates an intense particle circulation (see particle circulation patterns in Figs. 1(c1, c2)). The fluid above the bed surface is typically free of particles (see the gas fraction distributions in Figs. 1(b1, b2)). In the trailing wake of the bubbles, particles move upwards. The bubble movement leads to intense gas and particle axial mixing. Bubble dynamics can be investigated with non-intrusive laser based techniques [11], while magnetic resonance (MR) and magnetic particle tracking (MPT) can assess particle velocities [12, 13].

The fluidized state includes three different regimes: stationary bubbling fluidized bed, turbulent fluidized bed and the regime of fast fluidization. Although technological processes are recently being carried out in the last two regimes, the bubbling fluidized bed shown in Fig. 1 is of main interest for the present investigation and best fits the characteristics mentioned in the foregoing paragraphs. The prominent difference between the bubbling fluidized bed and the other two regimes is the existence of large bubbles and a clearly outlined free bed surface. Bubbles in FBs appear after the minimum fluidization velocity is reached. They are initially spherical but, as they grow, take shapes typical of gas bubbles in liquids —with concave bottoms (see Figs. 1(a1, a2)).

Depending on particle sizes, bubbles can be "fast" and "slow", resulting in bubble velocities higher or lower than the minimum fluidization velocity. In FBs with small particles (i.e. materials of the group B

according to the Geldart [14] classification), bubbles are fast. In FBs with large particles (materials of the group D [14]), bubbles are slow. Fast bubbles traverse the fluidized bed with very low mass exchange between the gas in the bubble and the gas in the emulsion (dense) phase.

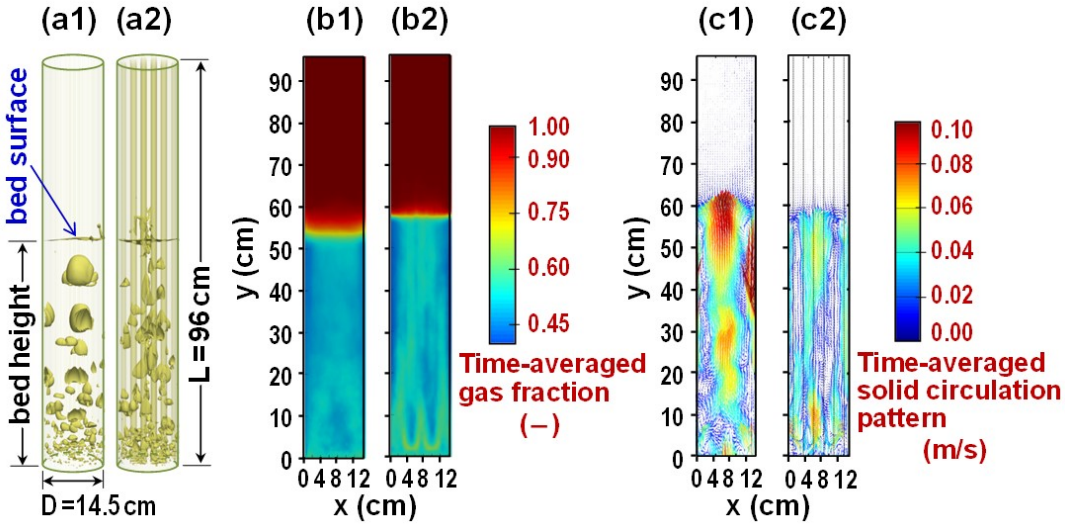


**Fig. 1.** Simulations in a fluidized bed without embedded vertical cooling tubes (a1, b1, c1) and with embedded vertical cooling tubes (a2, b2, c2). The configurations in (a1, a2) are used at PSI for biogas methanation [10]. (a1, a2) instantaneous 3D bubble contours, (b1, b2) time averaged porosity (gas fraction), and (c1, c2) time averaged circulation patterns of the solid (color denotes the magnitude of the solid velocity). The ratio of the superficial gas velocity to the minimum fluidization velocity is 4.5. Adapted from [9].

# 2 Context

## 2.1 Background / State of the art

As the project heavily focuses on model development, a short review is provided next on state-of-the-art models used in FBs. Models aiming at laboratory or industrial sizes employ (due to prohibitive computational costs) a “continuum” approach for at least one of the two phases, meaning that details such as particle-particle or fluid-particle interactions are typically volume averaged. Eulerian or Lagrangian models are adopted for the hydrodynamics of the gas and solid phases, as depicted in Table 1. A graphical representation of the employed models is further illustrated in Fig. 2. A summary of the models 1-4 in Table 1 (excluding Model 5, which is only applicable to colloidal systems) is provided below, considering at this stage only hydrodynamics (no chemical reactions).

| Model type | Solid phase | Gas phase | Coupling gas-solid | Scale |
|---|---|---|---|---|
| **1.** Discrete bubble model | Eulerian | Lagrangian | Drag closures for bubbles | 10 m |
| **2.** Two-fluid model | Eulerian | Eulerian | Gas-solid drag closures | 1 m |
| **3.** Unresolved discrete particle | Lagrangian | Eulerian (unresolved) | Gas-particle drag closures | 0.1 m |
| **4.** Resolved discrete particle | Lagrangian | Eulerian (resolved) | Boundary condition at particle surface | 0.01 m |
| **5.** Molecular Dynamics | Lagrangian | Lagrangian | Elastic collisions at particle surface | < $10^{-3}$ m |

**Table 1.** Types of models in dense gas-solid flows for gas fluidization (adapted from [15]).

### 2.1.1 Two fluid model (TFM)

These are Eulerian/Eulerian solid/gas models, whereby both phases are considered as interpenetrating continua. The gas and solid phases are described by a generalized form of the Navier–Stokes equations. The continuity and momentum equations for the gas-phase are [16, 17]:

$$\partial_t(\varepsilon_g\rho_g) + \nabla\cdot(\varepsilon_g\rho_g\boldsymbol{u}_g) = 0, \quad (1)$$

$$\partial_t(\varepsilon_g\rho_g\boldsymbol{u}_g) + \nabla\cdot(\varepsilon_g\rho_g\boldsymbol{u}_g\boldsymbol{u}_g) = -\varepsilon_g\nabla p_g - \nabla\cdot(\varepsilon_g\bar{\boldsymbol{\tau}}_g) - \varepsilon_g\rho_g\boldsymbol{g} - \boldsymbol{f}_d, \quad (2)$$

with the subscript $g$ denoting gas, and $\varepsilon_g, \rho_g, p_g, \boldsymbol{u}_g$ the local gas porosity, density, pressure and velocity, respectively, $\bar{\boldsymbol{\tau}}_g$ the viscous stress tensor, $\boldsymbol{g}$ the gravitational acceleration, and $\boldsymbol{f}_d$ the force due to momentum exchange between gas and solid. The momentum equation for the solid is [15]:

$$\partial_t(\varepsilon_s\rho_s\boldsymbol{u}_s) + \nabla\cdot(\varepsilon_s\rho_s\boldsymbol{u}_s\boldsymbol{u}_s) = -\nabla p_s - \nabla\cdot(\varepsilon_s\bar{\boldsymbol{\tau}}_s) - \varepsilon_s\rho_s\boldsymbol{g} + \boldsymbol{f}_d - \varepsilon_s\nabla p_g, \quad (3)$$

with the subscript $s$ denoting solid properties, in a manner analogous to $g$ in Eq. (2). Since the concept of particles does not exist within the TFM continuous model, the effect of particle-particle interactions is included indirectly via the effective solid pressure $p_s$ and effective solid stress tensor $\bar{\boldsymbol{\tau}}_s$.The gas solid force term $\boldsymbol{f}_d$ in Eqs. (2) and (3) can be approximated for monodispersed particles as:

$$\boldsymbol{f}_d = \beta(\boldsymbol{u}_g - \boldsymbol{u}_s), \quad (4)$$

with $\beta$ a momentum exchange coefficient. Semi empirical correlations are used for Eq. (4), e.g. by Ergun [18] and Wen and Yu [19]. More elaborate expressions have been developed [20] by fitting results of detailed drag force predictions using resolved discrete particle models (discussed in the coming Section 2.1.4). A closure is necessary for the solid pressure $p_s$ and the effective solid stress tensor $\bar{\boldsymbol{\tau}}_s$ (which in turn requires closures for the effective shear and bulk solid viscosities, $\mu_s$ and $\lambda_s$). State of the art closures are achieved from the kinetic theory of granular flow (KTGF), which calculates the energy dissipation in collisions via the Enskog theory. In KTGF the solid pressure and effective shear and bulk solid viscosities can be described in terms of the solid's volume fraction $\varepsilon_s$, the coefficient of normal restitution $e$, and the average granular temperature $\theta = <\boldsymbol{C}_p\cdot\boldsymbol{C}_p>/3$ with $\boldsymbol{C}_p$ the particle fluctuation velocity. KTGF models are still under development [21]. TFM/KTFG model simulations are shown in Figs. 3(a1-a3) for a 15 cm x 60 cm fluidized bed with 4 mm diameter glass particles in air, illustrating the effect of the normal restitution coefficient $e$ [15].

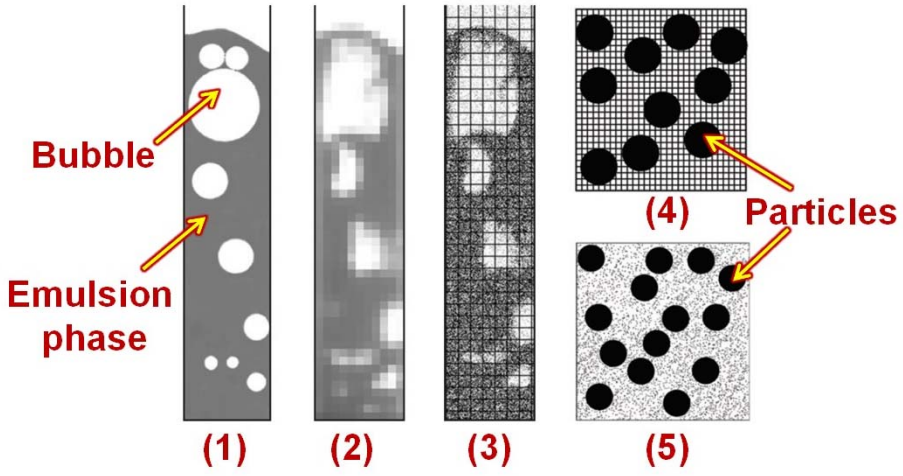


**Fig. 2**. Graphical interpretation of models 1-5 of Table 1 (adapted from [15]). For real sized fluidized beds, models 1-3 can be used. Model 4 is computationally tractable only for small representative parts of the FB, while model 5 is applicable only for very small (colloidal) systems.

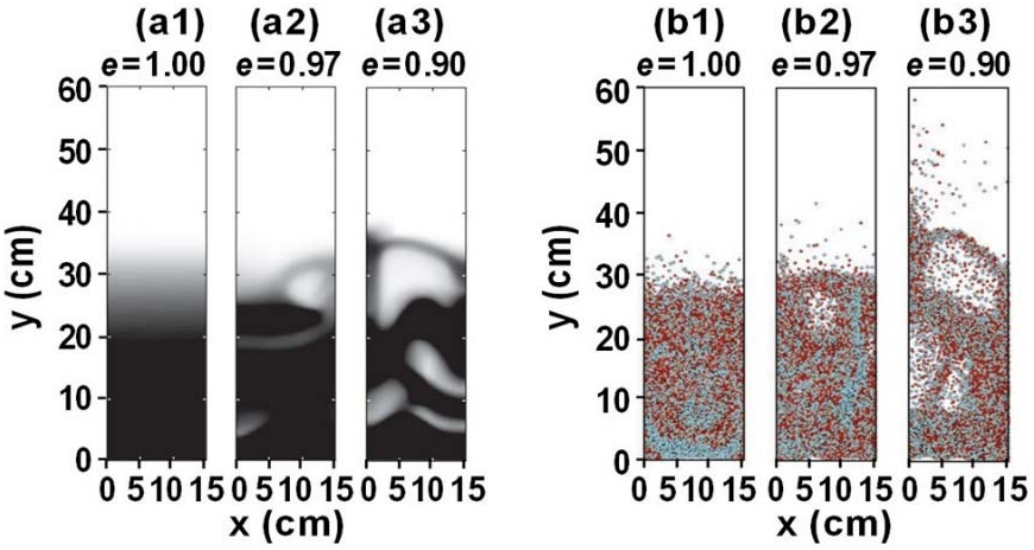


**Fig. 3.** (a1-a3) Snapshots of three different two fluid model (TFM) simulations for a quasi 2D fluidized bed (15x60 cm$^2$) of 4 mm diameter glass particles in air, showing the effect of the normal restitution coefficient $e$: gray shades indicate solid porosity $\varepsilon_s$ (brighter color is higher porosity), (b1-b3) snapshots of particle distributions in the same fluidized bed, using the unresolved discrete particle model (UDPM). Snapshots selected to correspond to the highest degree of heterogeneity. Adapted from [15].

### 2.1.2 Unresolved discrete particle model (UDPM)

In UPDMs (also called discrete element models, DEMs) the Eulerian grid is about an order of magnitude larger than the particle size, such that, as far as the gas phase is concerned, the particles only act as point sources or sinks of momentum. Nonetheless, as the solid phase follows a Lagrangian description, the particles occupy a finite volume and interact via collision rules. Most UDPMs for gas-fluidized beds use a CFD-type discretization for the gas phase [22].

The gas-phase follows the Eulerian description of Eqs. (1)-(2). The Lagrangian solid involves either a hard-sphere or a soft-sphere particle collision model. In a soft sphere model, the motion of a single spherical particle $a$ with mass $m_a$ and position vector $\boldsymbol{r}_a$ is given by Newton's second law:

$$m_a d^2\boldsymbol{r}_a/dt^2 = \boldsymbol{F}_{contact,a} + \boldsymbol{F}_{ext,a} + \boldsymbol{F}_{pp,a}, \quad (5)$$

where $\boldsymbol{F}_{contact,a}$ is the total contact force, consisting of the individual contact forces exerted by all other particles in contact with particle $a$. $\boldsymbol{F}_{ext,a}$ is the total external force ( = $\boldsymbol{F}_{g,a} + \boldsymbol{F}_{drag,a} + \boldsymbol{F}_{lift,a}$) that includes the gravitational force $\boldsymbol{F}_{g,a} = m_a\boldsymbol{g}$ and the forces exerted by the surrounding gas (drag $\boldsymbol{F}_{drag,a}$ and lift $\boldsymbol{F}_{lift,a}$, arising from the surface friction and pressure gradient). Finally, $\boldsymbol{F}_{pp,a}$ is the sum of all other particle-particle forces such as short-range cohesive forces due to van der Waals interactions between the molecules of the particles as well as long-range electrostatic forces. Figure 3(b1-b3) illustrates UDPM simulation results (same conditions as the TFM simulations in Figs. 3(a1-a3)) using 7'200 individual particles [15].

### 2.1.3 Discrete bubbles model (DBM)

At the Universities of Twente/Eidhoven, Netherlands, an alternate approach is being pursued to capture large-scale flow structures [23, 24]. The bubbles are considered as discrete entities, leading to the discrete bubble model (DBM), which originates from the modeling of gas–liquid bubble columns. In DBM the emulsion phase is modeled as a continuum and the larger bubbles as discrete bubbles. This model is not frequently used and requires further development in the laws for bubble breakup and coalescence. For this reason, this model is not elaborated herein.

### 2.1.4 Resolved discrete particle model (RDPM)

These are fully resolved simulations for both the gas and solid phases, applied only to small domains. Crucial in RDPMs is the correct implementation of the stick boundary condition. Lattice Boltzmann (LB) methods meet this requirement, by applying a modified bounce-back boundary condition [25]. Stick boundary conditions in a classical CFD approach for the gas can be applied by the immersed boundary (IB) method [26] along with a direct forcing method [27]. Interactions between gas and solid are accounted for by a force density $\boldsymbol{f}_{s\to g}$ added in the gas-phase momentum equation:

$$\partial_t(\rho_g \boldsymbol{u}_g) + \nabla\cdot(\rho_g \boldsymbol{u}_g \boldsymbol{u}_g) = -\nabla p_g - \nabla\cdot\bar{\boldsymbol{\tau}}_g - \rho_g \boldsymbol{g} - \boldsymbol{f}_{s\to g}. \quad (6)$$

Equation (6) is similar to Eq. (2), however, as the gas phase is fully resolved, the local gas porosity $\varepsilon_g$ does not appear in Eq. (6). Considering a spherical particle $a$, $\boldsymbol{f}_{s\to g} \equiv \boldsymbol{f}_{a\to g}$. The force density $\boldsymbol{f}_{a\to g}(\boldsymbol{r})$ in the Eulerian framework of Eq. (6) is calculated from the force densities $\boldsymbol{f}_m$ at the location of the Lagrangian force points $m$ falling within the range of influence of $\boldsymbol{r}$. The $\boldsymbol{f}_m$ can be calculated from the constraint that the local gas velocity should match the local particle velocity, leading to [15]:

$$\boldsymbol{f}_m = \frac{1}{\delta t}[\rho_m(\boldsymbol{U}_m - \boldsymbol{W}_m)]\left[\pi\left(12\frac{R^2}{\Delta^2}+1\right)/3N\right], \quad (7)$$

where $\boldsymbol{U}_m$ and $\rho_m$ are the initial gas velocity and density, respectively, at the Lagrangian point $m$, $\boldsymbol{W}_m$ the velocity of each force point $m$, and $\Delta$ the linear dimension of a CFD grid cell. The force acting on a particle $a$ is calculated as $\boldsymbol{F}_{g\to a} = -\sum_m^N \boldsymbol{f}_m \Delta^3$, which is then added to the right side of the particle's motion law (Eq. (5)). The solid is treated by the Lagrangian method, as described in the foregoing Section 2.1.2. RDPMs are mainly used to obtain realistic estimates of the gas-solid forces $\boldsymbol{F}_{g\to a}$, which can then improve the TFM and UDPM unresolved models.

Fully-resolved 3D simulations, using a CFD code with the immersed boundary (IB) method, are shown in Figs. 4(a1, a2) for monodispersed rigid spheres [28]. Goal is to compute the drag force, in order to improve closures for $\boldsymbol{f}_d$ in Eq. (2). A packing of 108 monodispersed rigid spheres with diameters $d_p$ =1.6 mm is used in Fig. 4(a1) with a solid fraction $\phi$ = 0.40. The second application in Figs. 4(b1, b2) refers to bi-dispersed spherical particles [29] whereby the LB methodology is used [25]. Figure 4(b1) illustrates a 3D configuration comprising 24 large and 192 small spheres. The total solid fraction is $\phi$ = 0.50, the diameter ratio $d_{p,2}/d_{p,1}$ = 0.50, and the solid fraction ratio $\phi_1/\phi_2$ = 1. The ratio of the particle force $\boldsymbol{F}_a$ ($a$ =1, 2), normalized by the mass-weighted average force $\boldsymbol{F}$ is plotted in Fig. 4(b2) versus the function $(1\text{-}\phi)y_a + \phi\, y_a^2$, where $y_a = d_{p,a}/\langle d\rangle$ with $\langle d\rangle$ the volume-averaged particle diameter. The simulation data (circles in Fig. 4(b2)) suggest a linear correlation for the particle force.

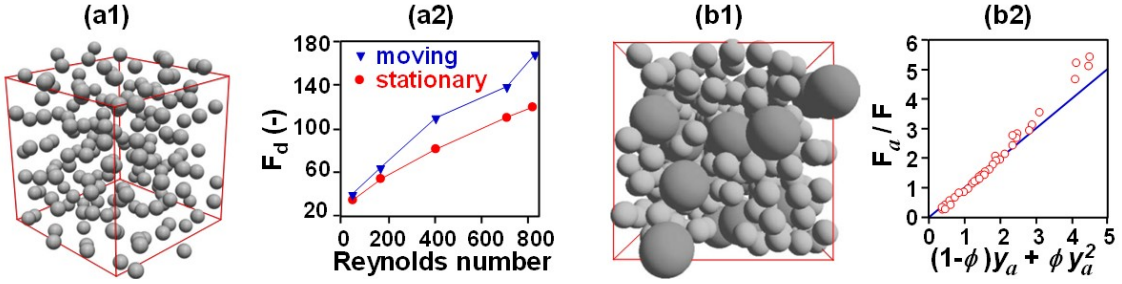


**Fig. 4.** (a1, a2) Fully resolved simulations of monodispersed rigid spherical particles, adapted from [28]. (a1): random particle configuration in a 3D domain, 108 spheres with $d_p$= 1.6 mm, (a2): dimensionless drag force as a function of Reynolds number based on the superficial velocity, stationary vs. moving spheres. (b1, b2) Fully resolved simulations of bi-dispersed rigid spheres, adapted from [29] (b1) 3D configuration, 24 large and 192 small spheres, total solid fraction $\phi$ = 0.50, $d_{p,2}/d_{p,1}$ = 0.50, solid fraction ratio $\phi_1/\phi_2$ = 1, (b2) normalized drag (simulations: circles, fit: line) versus a function of the total solid fraction $\phi$ and the ratio $y_a = d_{p,a}/\langle d\rangle$.

## 2.2 Motivation of the project

To set the motivation of the project, a brief summary is given below on the biogas methanation FB experimental and numerical activities at PSI.

### 2.2.1 Status of experimental work at PSI

Gas–solid fluidized bed reactors are used in the methanation of coal-derived synthesis gas. Typically, methanation on Ni catalysts is performed between 250 and 450 °C. The key chemical reactions are:

$$3\,H_2 + CO \leftrightarrow CH_4 + H_2O \qquad \Delta H_R^o = -206.28\ \text{kJ/mol}, \qquad \text{(R1)}$$

$$CO + H_2O \leftrightarrow CO_2 + H_2 \qquad \Delta H_R^o = -41.16\ \text{kJ/mol}, \qquad \text{(R2)}$$

$$2\,CO \leftrightarrow C + CO_2 \qquad \Delta H_R^o = -172.54\ \text{kJ/mol}, \qquad \text{(R3)}$$

where R1 is the methanation, R2 the water gas-shift, and R3 the Boudouard reaction (R3 is important only for low $H_2$/CO ratios). The exothermicity of all reactions requires efficient heat removal and this can be achieved with vertical cooling tubes [5], as shown in Fig. 1(a2).

Experiments at PSI pertaining not to the large FBs of Figs. 1(a1, a2) but to a smaller unit (diameter 52 mm and height 145 mm) are discussed next. An axially-traversable sampling probe/thermocouple measured the species compositions and temperature. The inlet gas comprised $H_2$, CO (at a stoichiometric methanation ratio $H_2$/CO = 3) and $N_2$ dilution. Commercial Ni/$\gamma$-$Al_2O_3$ catalysts were used (50 wt% Ni/$Al_2O_3$, BET 183 $m^2$/gr). The particles were of Geldart B type, with ***internal porosity in excess of 50%.*** Such a large porosity of the particles has modeling implications (see next section). The size distribution and morphology measured with laser diffraction and SEM, respectively, of the bare $\gamma$-$Al_2O_3$ particles without Ni is depicted in Fig. 5(a).

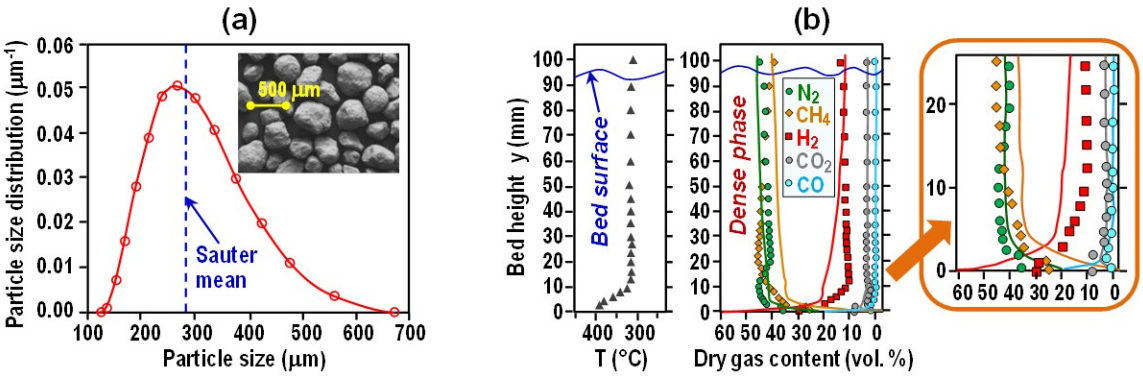


**Fig. 5.** (a) Size distribution of $\gamma$-$Al_2O_3$ particles of PSI's methanation bed (Sauter mean size of 290 μm) and particle morphology (adapted from [5]), (b) temperature and vol. composition along the bed (symbols: measurements, lines: predictions) for a case with 100 gr catalyst and inlet flow 10 nL/min (adapted from [30].

Measured and predicted (using PSI's macroscopic numerical model, which is described in the coming section) chemical compositions as well as measured temperatures are shown in Fig. 5(b) for a case with 100 gr catalyst, inlet flowrate 10 nL/min and pressure 1.3 bar. The methanation reaction (CO and $H_2$ conversion to $CH_4$) is largely completed in the first 20 mm. Deviations between measurements and predictions at heights up to 30 mm (see details in rightmost plot of Fig. 5(b)) bear, among other issues, the fact that the experiments probe mostly the dense phase and that the mass transfer between dense phase and bubbles is weak in the lower parts of the bed.

2.2.2 Status of numerical work at PSI

Apart from PSI's modeling, international works that simulated PSI's experiments are also provided in this section. Liu and Hinrichsen [31] used 2-D and 3-D two-fluid-models for methanation beds with Ni/$\gamma$-$Al_2O_3$ catalytic particles, with R1 and R2 kinetic rates taken from PSI [32], and they simulated the experiments at PSI shown in Fig. 5(b). The predicted time-averaged distribution of $H_2$ is shown in Fig. 6(a1), while comparisons between measurements and simulations are shown in Fig. 6(a2). Although the model predictions in Fig. 6(a2) are in better agreement with the experiments compared to the PSI model predictions in Fig. 5(b), discrepancies at the bed bottom are still evident (see enlarged graph in Fig. 6(a2)).

**The models developed at PSI** [30] (simulations in Fig. 5(b)) belong to the TFM class. Main simplifications include steady-state and one-dimensionality. Key model assumptions are [30]:

**a)** The gas chemical composition in the emulsion phase were the same as that inside the porous particles.
**b)** The bubble (gas) and emulsion phases were treated as plug flows (axial dispersion is not considered).
**c)** Methanation and water-gas-shift reactions were included, while the measured temperature profile (see Fig. 5(b)) wan an input to the model, negating solution of the energy equation.
**d)** The gas flow rate through the dense phase was constant. Because of volume contraction in the dense phase due to the methanation reaction, an extra convective mass transfer (bulk flow) from the bubble phase into the dense phase was introduced.

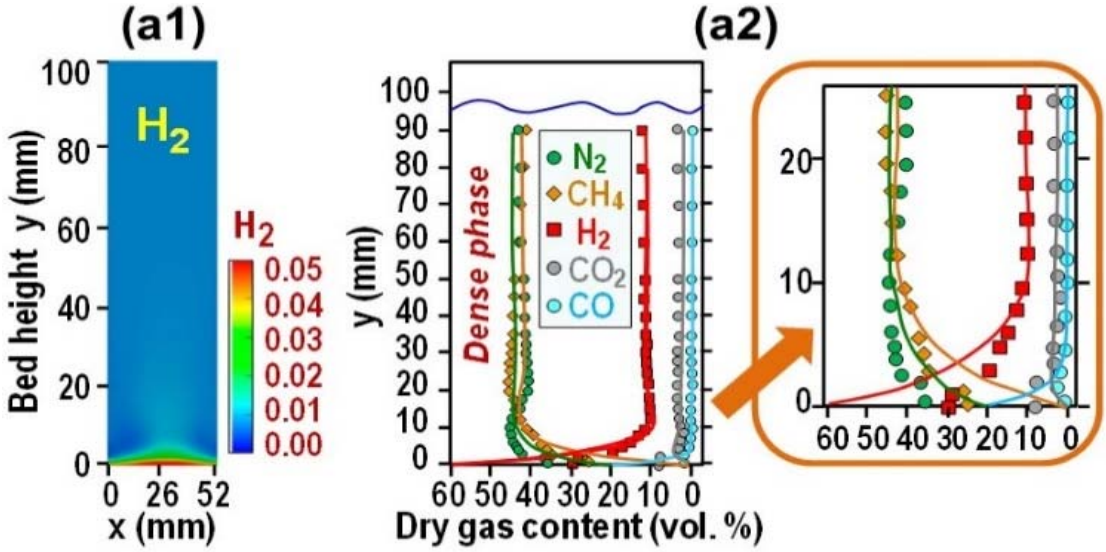


**Fig. 6.** (a1, a2) Simulations of PSI's methanation fluidized bed (operating conditions as in Fig. 5(b)) using a two-fluid-model (TFM): (a1) time-averaged $H_2$ mass fraction distribution and (a2): volumetric chemical composition along the bed (symbols: measurements, lines: predictions). Adapted from [31].

**Assumption (a)** deserves special attention. As the catalytic particles have an average porosity of about 50% and, when considering the void fraction of the fixed bed (before the onset of fluidization), it can be estimated that the ***gas inside the particles constitutes about 25% of the gas*** in the entire bed. Depending on the relative rates of interphase transport (between the gas external to the particle and the particle outer surfaces), intra-particle transport (within the gases inside the particle), and

chemical reactions, large composition differences of the gas inside and outside the particles may occur.

**Assumption (b)** is also questionable since the rate of transport of intra-particle gas to the exterior particle surface could be slow with respect to the axial convective transport, thus inducing an appreciable axial dispersion. The multidimensional TFM and UDPM models (Sections 2.1.1 and 2.1.2) do not account for a second category of gas different from the local gas of the emulsion phase. Of prime interest is to assess the impact of the gases trapped inside the porous solid by carrying out resolved simulations of a single particle and of particle clusters. The results of such resolved simulations may point to the need of extending PSI's TFM model from two to three phases (solid phase, conventional gas phase of the bubbles, and another gas phase inside the particles).

## 2.3 Goals

**Main goal is to develop a numerical code based on a resolved discrete catalytic porous particle methodology for investigating the physicochemical processes at the particle scale and for advancing large-scale models used for simulation of biogas methanation fluidized beds.** Previous works have investigated single or small groups of catalytic porous particles or pellets, which were however stationary. These works assessed intra-particle reaction and diffusion, using statistical description for the pore network, with 1D or 2D CFD codes [33-35]. Nonetheless, statistical descriptions based on volume-averaging for particles down to 150 μm (Fig. 5(a)) are not warranted given the potentially limited number of large pores (the average pore size of the particles is ~10 μm, assessed by BET**).** 3D reacting simulations of a catalytic particle with a detailed internal porous description and particle movement in a flow with chemical composition relevant to fluidized beds have not yet been reported. Specific goals of the proposed work are:

-Develop a 3D lattice Boltzmann (LB) thermal model, which can accurately describe the detailed interactions of the catalytic solid particles and the gaseous flow in Fluidized Beds (FBs).
-Validate the model with experiments at PSI's biogas methanation FB. The model will include the detailed porous geometry of the $Ni/Al_2O_3$ catalytic particles (obtained with X-ray tomography) and realistic methanation catalytic kinetics at the external and internal surfaces of the porous particles.
-Assess the extent of "axial dispersion" induced by the trapping of gases inside the porous network of the solid FB particles.
-Use the developed model to simulate new biogas methanation experiments at PSI's test rig and to optimize the FB design for this process.
-Advance not only the FB models related to biogas methanation but also FB models relevant to other energy conversion processes such as coal and biomass gasification.

### 2.3.1 Expected results

- Construct a validated 3D LB model for the detailed two-phase flow (solid/gas) interactions in fluidized beds, including catalytic reactions at the particle surfaces with specific kinetics referring to the biogas methanation process.
- Characterize with X-ray tomography the porous internal structure of the catalytic particles.
- Provide a conclusive answer to the fundamental question regarding the impact of the gases trapped inside the porous structure of the rising solid particles on the performance of biogas methanation processes.
- Using the developed LB model, construct a validated large-scale macroscopic model for the entire FB, which is applicable not only to methanation FBs but also to FBs used in other

energy conversion processes (biomass and coal gasification, Fischer-Tropsch synthesis).
- Optimize the biogas methanation FB test-rig at PSI using the above-developed models.

Due to personnel changes at PSI that have been communicated to BfE, the revised goals reported for this project, were the following:

- Construct a validated 3D LB model for the detailed two-phase flow (solid/gas) interactions in fluidized beds, including of catalytic reactions at the particle surfaces with specific kinetics referring to biogas methanation process.
- Apply the newly developed LB model for a test case of methane total oxidation.
- Characterize with X-ray tomography the porous internal structure of the catalytic particles.

# 3 Approach and methodology

## 3.1 Modeling approach

Figure 7(a), delineates four main domains in fluidized beds (bubble, wake, cloud and emulsion). The *bubble*s contain very small amounts of solids. Each gas bubble has a wake that contains a significant amount of solids. As the bubble rises, it pulls up the wake with its solids behind it. The net flow of the solids in the *emulsion* phase is therefore downwards. The gas within a bubble remains largely within that bubble, only penetrating a short distance into the surrounding emulsion phase. The region penetrated by gas from a rising bubble is called the *cloud* (Fig. 7(a)). Of specific interest in this work are the two domains where most of the solid resides (emulsion and wake).

The emulsion phase exists at minimum fluidizing conditions. The gas occupies the same void fraction in this phase as it had in the entire bed at the minimum fluidization point. In addition, because the solids in the emulsion phase are flowing downwards, the minimum fluidizing velocity $u_{mf}$ refers to the gas velocity in the emulsion, $u_e$, relative to the moving solid particles velocity $u_s$:

$$(u_{mf}/\varepsilon_{mf}) = |u_e| - |u_s|, \tag{8}$$

where the porosity at minimum fluidized velocity, $\varepsilon_{mf}$, enters Eq. (8) since the superficial velocity $u_{mf}$ is based on the empty FB cross section. For the downward particle velocity $u_s$ in the emulsion, engineering correlations are available [36]. Velocities of 0.1 to 1.0 m/s have been observed [37].

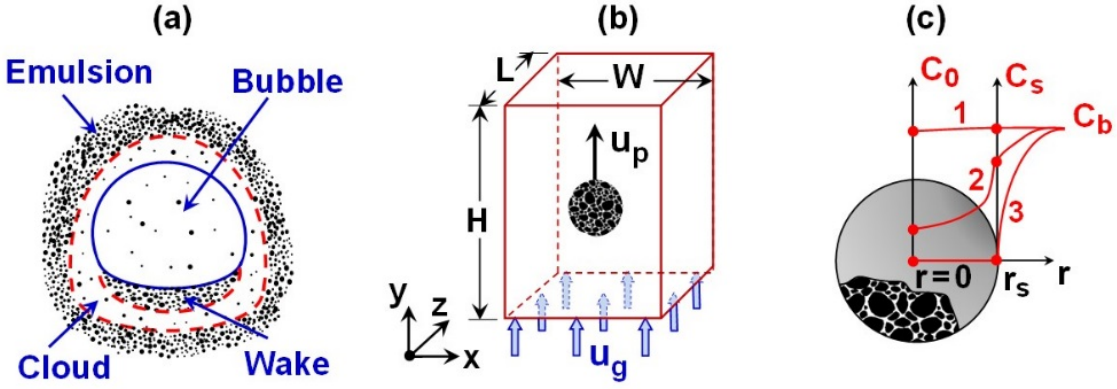


**Fig. 7**. (a) Domains of gas and solid in fluidized beds, (b) simulation domain for a single spherical porous catalytic particle, (c) potential reactant profiles in a porous catalytic particle: $C_b$ is the bulk concentration, $C_s$ the concentration at the external surface ($r = r_s$) and $C_0$ the concentration at the particle center ($r = 0$).

In the wakes, the concentration of solids is equal to the concentration of solids in the emulsion phase, and hence the gaseous void fraction in the wake is also the same as in the emulsion phase. Because the emulsion phase is at the minimum fluidizing condition, the void fraction in the wake is equal to $\varepsilon_{mf}$. The average velocities of both solid and gas in the wake are considered to be the same and equal to the upward velocity of the bubbles $u_b$ [36]. The bubble velocity, $u_b$, can in turn be estimated from engineering correlations based on the inlet gas velocity at the distributor plate $u_0$, the minimum fluidized velocity $u_{mf}$ and an appropriately-defined representative bubble diameter $d_b$ [38]:

$$u_b = u_0 - u_{mf} + 0.71\sqrt{g d_b}. \tag{9}$$

Simulations will be initially performed for a single catalytic particle with its entire internal 3-D porous network, which will be assessed by X-ray tomography at PSI's Synchrotron Light Source (SLS). The particle will be embedded in a 3D simulation flow domain $H \times L \times W$ (a few mm for each dimension) as

shown in Fig. 7(b). Relevant values for the inlet gas velocity $u_g$ at $y$ = 0 in Fig. 7(b) and for the initial particle velocity $u_p$ in Fig. 7(b) can be computed for PSI's methanation FB using Eqs. (8) and (9). In PSI's experiments $u_{mf}$ ~ 3 cm/s [30], while the upward gas velocities and downward solid velocities in the emulsion phase fall in the ranges 20-40 cm/s and 10-30 cm/s, respectively. For the wake phase, concurrent upward gas and particle velocities are 30-60 cm/s. Initial gas-species compositions in the *H*×*L*×*W* domain as well as inside the particle will be taken from measurements at various bed heights in Fig. 5(b). The simulations will be thermal for the solid and gas phases, with initial conditions defined by the measured local measured bed temperatures (Fig. 5(b)). Reactions R1 and R2 (methanation and water gas shift) will be considered, as the Boudouard reaction (R3) is important only for low $H_2$/CO ratios.

Mass transfer between the gas and the reacting solid will be investigated in the setup of Fig. 7(b). While for the particle-dense emulsion and wake regions the notion of a single particle in domains of a few mm$^3$ is not realistic, still fundamental processes occurring in the neighborhood of each particle will be be extracted. In Fig. 7(c) the profile of a reactant is plotted along the particle radius, showing: (1): kinetic limitations, (2): mixed kinetic and external/internal transport limitations, (3): external transport limitations. It is likely that such diverse solutions may occur at different bed heights and methanation operating conditions. Apart from studying the fundamental processes at the particle level, an important outcome of this part was the assessment of ***composition differences between the gas inside the particle and the surrounding gas***. This has profound implications, as current modeling [30] considers (at a given bed height) no composition differences between the gas inside and outside the particles in the emulsion phase. Such a modeling assumption requires careful assessment, as the intra-particle gas occupies a significant fraction of the total bed volume (~25%).

In a second phase (planned with a new postdoctoral student), multiple catalytic particles (MCP) in the *H*×*L*×*W* domain will be investigated, using realistic particle numbers (deduced from the experimental $\varepsilon_{mf}$ ~ 0.55) and size distributions (from Fig. 5(a)). Fully resolved multiple-particle simulations are computationally prohibitive. Therefore, instead of a detailed internal porous network, each particle class will be "trained" by the foregoing single-particle simulations to include a macroscopic description of the intra-particle diffusion and reaction processes.

### 3.1.1 Lattice Boltzmann methodology

Considering that a resolved discrete particle model (RDPM) model is to be employed, *two modules were constructed*, namely a solver for the multi-component species and thermal flow capable of handling catalytic boundary conditions, and a Lagrangian method to track the particles movement.

The lattice Boltzmann (LB) method can handle microscale systems without added difficulties with respect to solver stiffness and treatment of the no-slip boundary condition. Since the chemically reactive flow involves 6 species ($H_2$, CO, $CH_4$, $H_2O$, $CO_2$ and inert $N_2$) and two reactions (R1 and R2), the entropic multicomponent LB model which was enhanced at PSI to include catalytic boundary conditions [39-41] will be used. The model solves for the LB equations:

$$\partial_t f_{ij} + c_{ij\beta}\partial f_{ij} = -\frac{1}{\tau_1}\left(f_{ij} - f_{ij}^{*}\right) - \frac{1}{\tau_2}\left(f_{ij}^{*} - f_{ij}^{eq}\right), \tag{10}$$

where $f_{ij}$ are the distribution functions of species $j$ along the discrete lattice directions $i$ with lattice velocities $c_{ij\beta}$ ($\beta$ refers to $x, y, z$). Moreover, $f_{ij}^{eq}$ and $f_{ij}^{*,eq}$ are the equilibrium and quasi-equilibrium states for the distributions, and $\tau_1$ and $\tau_2$ are the relaxation times for the collision and relaxation towards $f_{ij}^{eq}$ and $f_{ij}^{*,eq}$, respectively. The density $\rho_j$, and velocity $u_{j\beta}$ for each species $j$ are then recovered as moments of $f_{ij}$:

$$\rho_j = \sum_i f_{ij}\,, \qquad u_{j\beta} = \sum_i f_{ij}\, c_{ij\beta} \,/\, \rho_j\,. \tag{11}$$

The maximum species molecular weight ratio in our application is 22 ($CO_2/H_2$) which can be accurately handled by the present LB model [40, 41] considering different values of $c_{ij\beta}$ for each species and using interpolation so as to adopt the same time and space discretization for all species. Having resolved the flow around a single or multiple particles, the net force acting on each particle was computed and used to determine the new position of each particle. The calculation of forces in the LB framework followed the momentum exchange scheme by Ladd [25].The obtained hydrodynamic forces along with the contact forces from particle collisions (the latter are considered only for the second phase with multiple particles), subsequently determined the evolution of particle velocity and position based on Newton's second law, i.e., by integrating Eq. (5) in time. The energy equation, is not included in the present model, but will be treated in the future with a passive scalar approach which would be decoupled from the LB framework, i.e. the thermal model will only require the velocities obtained from the LB part to solve an energy equation and update the temperature field.

### 3.1.2 Single catalytic particle (SCP) simulation

Figure 8(a) illustrates the computational domain and the solid structure studied in the single catalytic particle (SCP) problem. A generalized spherical form of the particle (still with external roughness) was initially selected, with the internal void structure (obtained by X-ray tomography) having an irregular shape (as e.g. in Fig. 8(b)). The spherical outer shape allowed an easier comparison of simulation results obtained with particles of different diameter; moreover, the actual particle shapes do not substantially deviate from the spherical geometry (see Fig. 5(a)). In conventional LB simulations on non-reacting surfaces, the treatment of the no-slip boundary condition was realized via the bounceback (BB) rule, which redirects those distribution functions $f_{ij}$ impinging on the solid wall to the opposite direction after collision. The BB rule on the curved external and internal particle surfaces, however, requires interpolation to reach second-order accuracy. This approach has been successfully used for the complex polydisperse particles in a 3-D stationary packed bed by Safi and Ashrafizaadeh [42] Extension of the BB rule for moving surfaces was proposed in [43].

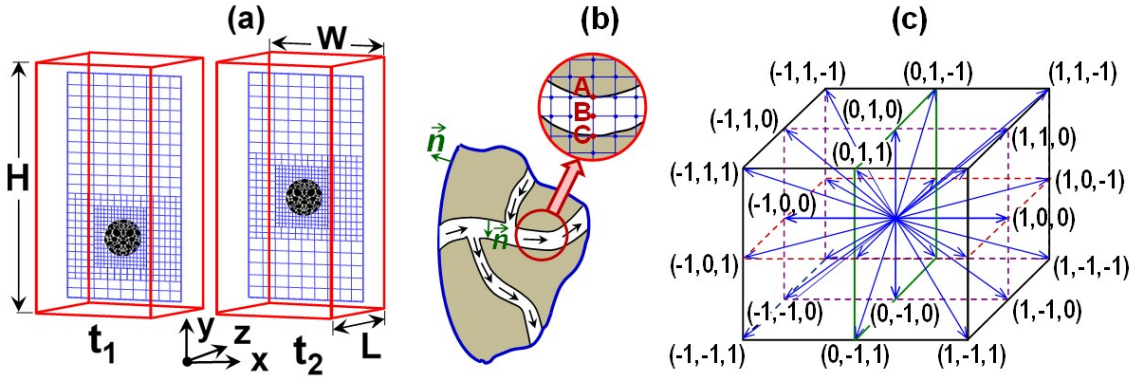


**Fig. 8.** (a) Illustration of a moving single particle and the adaptive LB mesh traveling with the particle, at times t1 and t2, (b) detail of the porous network of a catalytic particle, (c) D3Q27 LB lattice.

Catalytic boundary conditions were also applied on the particle external and internal surfaces. This was realized via the enhanced diffusive BB rule introduced by our group in Kang et al. [41] accounting for the change of species mole fractions $X_i$ as their corresponding distribution functions are modified during BB by considering the species fluxes in the direction $\vec{n}$ normal to the catalytic surface (Fig. 8(b)). Nevertheless, the methodology in [41] was originally given for stationary planar catalytic surfaces and needed modifications for moving objects with curved geometries.

The relative size of porous channel diameters $d_c$ and particle diameters $d_p$, was used to estimate the resolution of the underlying lattice and hence the required computational resources. In the methanation FB of interest, the Sauter-mean diameter value is 290 μm (Fig. 5(a)), while porous channels have a mean diameter $d_c$= 10 μm, as determined by BET at PSI. A minimum resolvable $d_c$ = 1 μm was herein adopted (given the adequate 0.32 μm resolution of the XTM technique). thus resolving the bulk of the internal porous volume. Even for $d_c$ = 1 μm, the flow still falls in the no-slip regime at atmospheric pressure. From the numerical point of view and the previous numerical experiments in porous media [44] we have established that 3 lattice nodes are still sufficient to cover $d_c$ (see Fig. 8(b) with points A, B, C) so as to accurately resolve the nearly creeping flow inside the smallest 1 μm pores without losing much accuracy.

Considering a 3-D stencil, e.g. D3Q27 (Fig. 8(c)), 6 chemical species, and cross-flow lengths of $L = W = 3d_p$ to $4d_p$, the above discussed requirement for the lattice resolution translated into hundreds of gigabytes of memory space and an enormous computational time –if a uniform lattice was to be used. In particular, for the SCP problem this requirement was only enforced by the internal porosity and external roughness of the particle, such that the rest of the $H \times L \times W$ domain will be resolved on lower resolutions. This motivated us to employ an adaptive mesh refinement (AMR) framework such that the lattice was only refined in a block surrounding the particle as depicted in Fig. 8(a). In the adopted AMR framework, interpolation was required to exchange data between the coarse and fine lattices, with a lattice spacing ratio larger than two. Multiple lattice levels were introduced to keep the data transfer between lattice levels smooth and to minimize numerical errors associated with interpolations. Similar strategies were also widely used in two-phase flow solvers [45]. Contrary to implementations with deformable interface shapes where a dynamic criterion determines the refinement pattern, the present problem enjoyed a fixed refining layout around the particle in a multi-block arrangement (Fig. 8(a)).

To address the computational needs of this methodology, parallel implementations were sought. Computer resources included multicore CPUs or GPGPUs, realized via the local dedicated computer cluster at Dr. Mantzaras' group with 72 high-end CPU cores and a total DRAM size of 1.5 TByte, in addition to a GPGPU-based cluster with 4 GPGPUs along with 24 CPU coresFor resolution requirements beyond the local PSI compute capabilities, porting the simulations to external high performance facilities was done, e.g. the state-of-the-art computer clusters in CSCS Mano, were used, offering a remarkable parallelization capability. This was possible via more than 5,000 GPGPU-enabled compute nodes in the Piz Daint supercomputer of CSCS.

### 3.1.3 Multiple catalytic particles (MCP) simulation

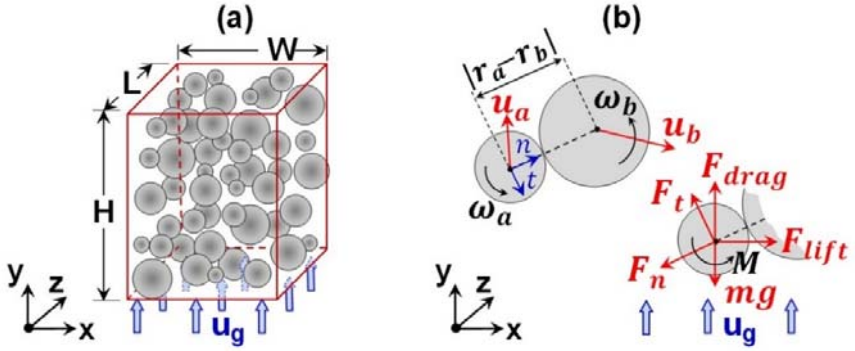


**Fig. 9.** (a) Representation of the multiple particle problem, (b) illustration of the particles arrangement at the collision moment (top, adopted from [78]) with different forces acting on a sample individual particle (bottom).

Having established the effect of the internal gas diffusion from the SCP, simulations will be carried out in the future for flow/diffusion/reaction in the multiple catalytic particles (MCP) problem as illustrated in Fig. 9(a). Therein, the internal particles porosity will be neglected and accounted for via a correction to the transport on the external particle surfaces, in order to render the computations feasible. Such corrections or equivalent macroscopic models have been recently proposed in [46]. The numerical procedure for MCP will be identical to that of SCP, except that a uniform lattice will be employed over the entire domain and a fully resolved discrete particle method (RDPM) will be exploited. Assuming a minimum of 5 lattice nodes to cover the diameter of the smallest particles, as established in [42] for a packed bed of stationary particles, a uniform lattice structure will allow for a number of particles ~$10^2$. Such particle numbers in lattices $H \times L \times W$ of a few $mm^3$ will be consistent with the emulsion phase porosities ~40-50% in the methanation FB.

To capture the inter-particle collisions in a Lagrangian fashion, the soft sphere model described in Section 2 will be adopted during the RDPM computations. As illustrated in Fig. 9(b), in addition to the lift $F_{lift}$ and drag $F_{drag}$ forces exerted by the gas and the gravity force $mg$, other major forces will include the contact forces $F_t$, $F_n$ along the tangential and normal directions, respectively, together with the moment $M$ which mainly arises due to $F_t$ at the contact point. The soft sphere model will be more affordable for a large number of particles and a dense system since, contrary to the hard sphere model, collisions are not instantaneous and need not to be treated in a serialized manner. Lastly, the model will intrinsically handle the collision of particles with different diameters ~150-550 μm, as assessed from the distribution of Fig. 5(a).

## 3.2 Experimental approach

The experimental methodology involved two tasks: a) characterization, by means of phase-contrasted X-ray tomographic measurements of the detailed porous structure of the $Ni/Al_2O_3$ catalytic particles a task carried out within this project and b) performing in the future additional experiments at the biogas methanation FB test rig of PSI, investigating different operating conditions (feed compositions, bed velocities), which will be an input for the LB model simulations.

Phase-contrasted X-ray tomography (XTM) of the $Ni/Al_2O_3$ solid particles was undertaken at the Synchrotron Light Source (SLS) of PSI, with the help of a beamline scientist (Dr. Anne Bonnin). Resolution of 0.16 μm was achieved, resulting in a maximum numerical resolution of 2x0.16 μm = 0.32 μm), which was sufficient to study solid particles with average size of 300 μm (see the particle size distribution in Fig. 5(a)) and internal pores with average sizes of ~10 μm. It is stressed that such high resolution was only possible via the phase-contrasted XTM methodology. In the past, similar resolution has also been obtained at SLS when measuring the porous structure of gas diffusion layers (GDLs) of polymer electrolyte fuel cells (PEFCs) [47].

# 4 Results

## 4.1 Simulations for 2D/3D static porous catalytic particles

As the first step towards constructing a solver for single catalytic particle, the existing 2D solvers for reactive surfaces at the CFG group were enhanced to include reactions not only for flat surfaces but for irregular and curved solid reactive surfaces as well. The difficulty in treating the latter case was in recovering the correct mass balance on a non-flat surface with regards to its true curvature and hence detecting the correct vector normal to the interface. This was realized by first finding the fluid points near the reactive surface whose LB distribution functions coming into the fluid zone were unknown at the end of each time step, as illustrated in Fig. 10(a). The average orientation of the incoming velocity vectors then defined the normal to the surface and hence the true direction of the mass fluxes. In the next step, the unknown distribution functions were calculated via an iterative scheme (initially proposed in [41] and modified in the present solver to balance the mass), which was based on the rate of reaction and the existing concertation of the different species. We very recently published this numerical method for irregular surfaces in another application dealing with water evaporation in the porous gas diffusion layers of Polymer Electrolyte Fuel Cells [48].

In order to validate and ensure the accuracy of the solver, we first applied the code to the rather standard benchmark problem of total catalytic oxidation of the methane gas ($CH_4$) at a constant particle temperature of $T_{part}$

$$CH_4 + 2O_2 \rightarrow CO_2 + 2H_2O \qquad r = A[CH_4]\exp(-E/RT_{part})$$

where $r$ is the reaction rate, $A$=1.27×10$^5$ cm/s, $E$=77 KJ/mol [49] is the apparent activation energy and $R$ is the gas constant. The setup can be seen in Fig. 10(b) and consisted of flow and reaction around a single 2D porous catalytic particle placed in the first quarter of a 2D planar channel with the upper and lower walls been non-catalytic. The entire system was kept at isothermal conditions with temperature equal to $T_{part}$=1200 K. The inlet gas was flowing at a velocity of $U_{in}$=1.2 m/s and comprised a mixture of oxygen and methane with molar concentrations of $X_{CH4}$=0.1 and $X_{O2}$=0.9. The particle was constructed to be porous by artificially carving small channels inside its volume in order to imitate the porous structure of realistic FB particles.

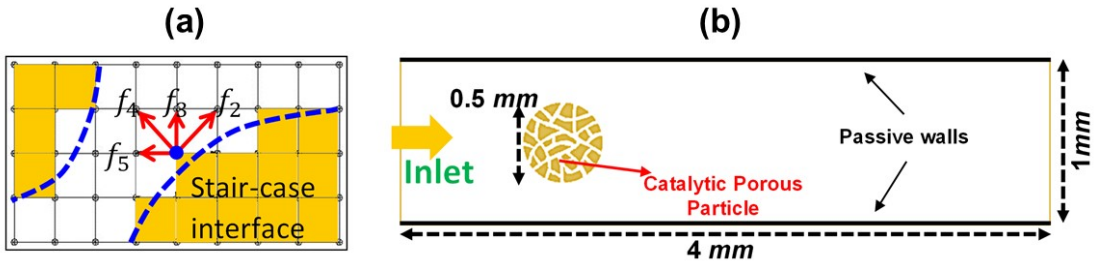


**Fig. 10.** (a) 2D problem defined for the static catalytic particle with arbitrary porosity, (b) illustration of the surface reconstruction and boundary conditions applied to the irregular catalytic surfaces inside the porous particle.

The problem was solved to the steady state, i.e. until there was no appreciable change in species concentration over the entire domain. Fig. 11 presents the mole fractions of the $CH_4$ fuel and $CO_2$ product around and inside the particle, while Fig. 12 shows the corresponding distribution of the total mixture velocity. It was evident that the flow could diffuse well inside the particle, although at a much lower velocity in the core of the porous structure. Nevertheless, the lower velocity corresponded to a

longer residence time of the fuel and oxygen, which in turn results in higher concentrations of products.

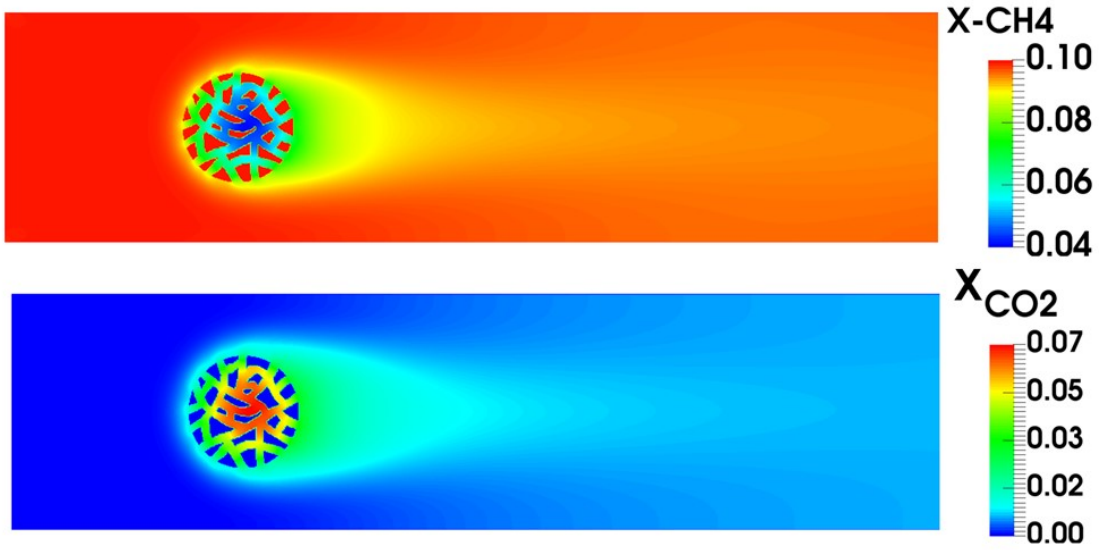


**Fig. 11.** Mole-fraction distribution of methane (up) and carbon dioxide product (bottom) over and inside the 2D static catalytic particle for the total oxidation of methane.

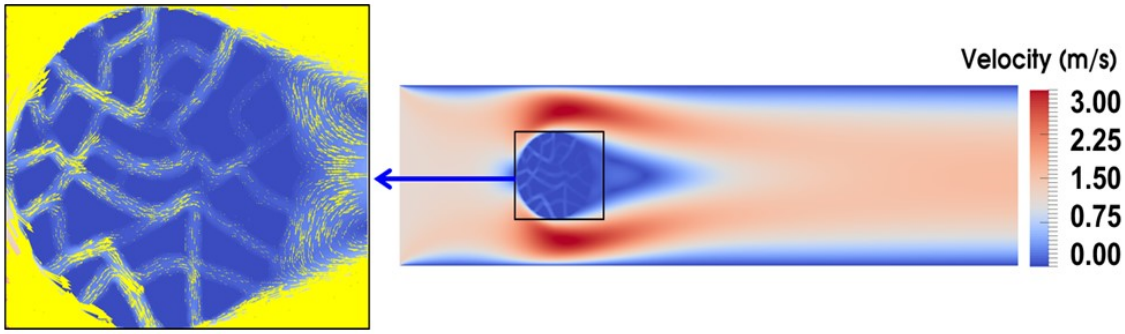


**Fig. 12.** Velocity distribution over and inside the 2D static catalytic particle

In the next step, and increasing the complexity, the previous benchmark problem was extended to 3D as illustrated in Fig. 13(a). Herein, a porous catalytic particle of the same size as in the 2D problem was constructed via an agglomeration of more than 100 smaller particles of different sizes in a random fashion (see Fig. 13(b)), so as to obtain a porosity of ~50%. This value was the average porosity of the catalytic particles in our methanation FB and bears a very high tortuosity as well. In order to accomplish the simulations within a reasonable time, the entire 3D computational domain was divided into 8 subdomains with equal sizes and the computations are distributed in parallel on 8 GPGPUs on CSCS's Piz-Daint cluster. Steady state solutions were then obtained within only 6 hours, thus allowing a great deal of time for post-processing of the results.

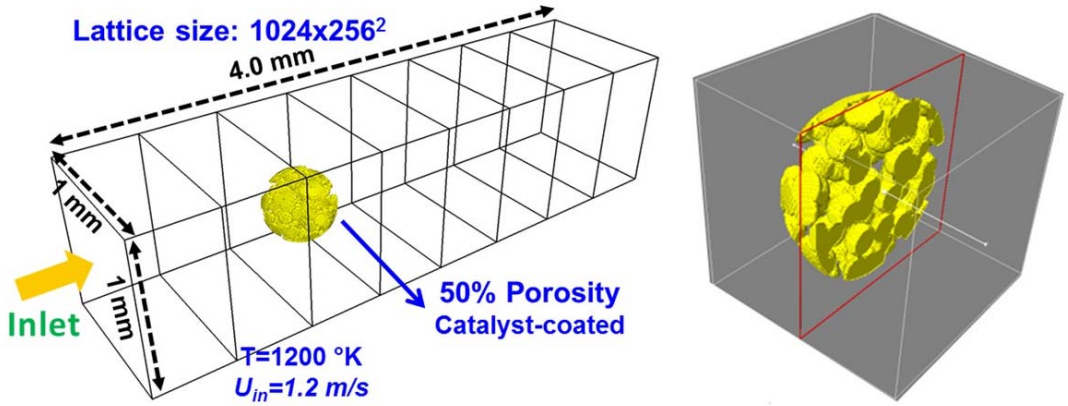


**Fig. 13.** (a) The 3D problem for 3D static catalytic particle arbitrary porosity. (b) Illustration of the 3D particles used in the simulations with ~50% porosity realized through agglomeration of smaller solid spherical particles.

Fig. 14 provides the flow streamlines around and inside the catalytic particles colored with the concentration of the fuel ($CH_4$) and product ($CO_2$). Despite the high tortuosity of the particle, the significant concentration of products (as seen for those streamlines at the particle core) revealed the contribution of the particle's internal porosity to the overall reaction performance. In general, the simulations showed that the mixture of reactants was first supplied to the particle via convective transport in the upstream front of the particle, whereas diffusive transport tried to create a rather uniform species distribution inside the particle such that reaction could take place due to the high residence time of the mixture. At the absence of large velocities inside the particle, diffusion carried the burnt gases towards the low velocity wake behind the particle. The circulating flow at the wake then enhanced the mixing with the fresh gas arriving from the particle sides, which in turn convected the products downstream and created a wake of high product concentration behind the particle.

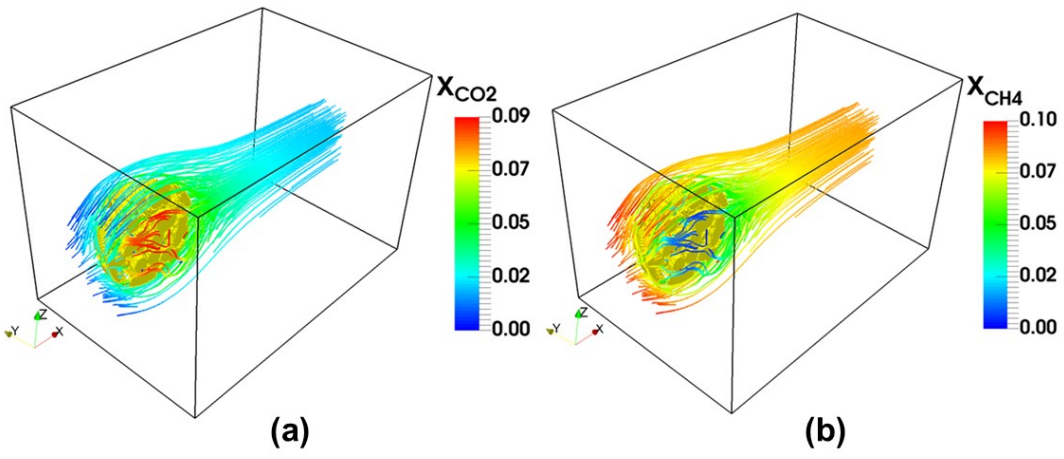


**Fig. 14.** Flow streamlines around and inside the 3D porous particle colored in concentration of (a) $CO_2$ and (b) $CH_4$. Note that the particle is cut in the X-Z plane for better visualization of the flow inside the particle.

## 4.2 Simulation of moving 3D porous catalytic particles

As in real operating FBs where particles are traveling with independent fluidization velocities, it was necessary to include the effect of a moving particle interacting with the surrounding fluid not only via chemical reaction but also via hydrodynamic forces (including drag force on the particle). To this end, the single catalytic particle used in the previous example was now assumed to have an initial velocity, which was different from that of the incoming flow of gas mixtures. The particle's velocity was hence reduced due to the drag forces arising from the difference between particle velocity and flow velocity. This was realized by applying the momentum exchange procedure to measure the total force exerted on the particle as the net momentum exchanged by the LB distribution functions at each fluid-solid contact outside and inside the particles, and then integrating over all contact points. Moreover, special attention was paid to avoid jump of the hydrodynamic properties and species concentrations as the boundary moved and left new fluid regions behind, as well as to transfer the particle geometry between the subdomains as the particle was moving across different subdomains along the channel length.

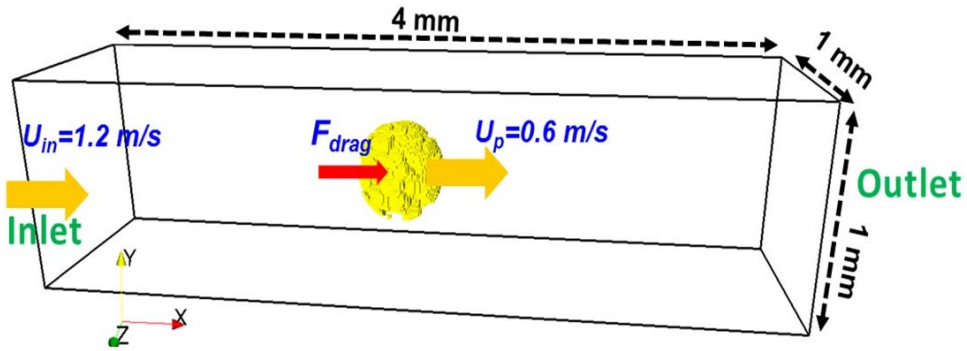


**Fig. 15.** Illustration of the problem for the 3D moving porous catalytic particle with arbitrary porosity. Note the different velocity of the flow and the particle.

The employed numerical setup is depicted in Fig. 15, in which the particle entered the 3D channel with the initial speed of 0.6 m/s, which was 50% of the flow velocity. The same benchmark catalytic reaction and inlet concentration of the reactants were considered at the inlet and the particle stayed inside the domain for ~6 ms until it exited the channel. The flow streamlines colored in $CO_2$ concentration are shown in Fig. 16 at 1 and 4 ms after the start of the simulations. It could be seen that the gases, which were rich in concentration of product species and were trapped inside the particles, were carried along with the particle as it moved forward. Moreover, compared to the stationary particle simulation in Fig. 14, the product distribution after 4 ms in Fig. 16(b) was extended over a larger area to left of the particle, i.e., the particle had left a large diffusive trace in the upstream direction since diffusion was strong enough to compete with the velocity (convection) of the flow relative to the moving particle. This revealed the true transient dynamics of the product distribution over time, which could be reproduced with stationary simulations.

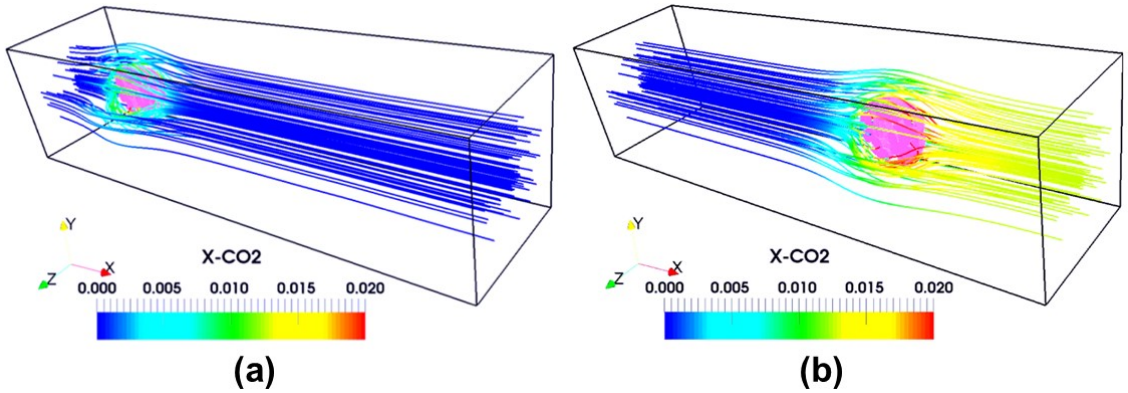


**Fig. 16.** Flow streamlines for the moving catalytic particle colored in the concentration of $CO_2$ at (a) 1 ms and (b) 4 ms after the start of the simulation. The particle moves from left to the right along the X axis.

## 4.3 X-ray tomography and data incorporation into simulations

Although the previous incorporation of artificially reconstructed porous particles helped understanding the interaction of convection/reaction/reaction over a particle, the solution still lacked the realistic geometry of the actual catalytic particles used in the FB experiments. This is indeed of paramount importance since apart from particle's porosity; the tortuosity of its porous network played a critical role in convection and diffusion inside the particle as some trapped gas may have not actively participated in the reactions due to poor connectivity or extremely low velocities of the gas in the individual pores.

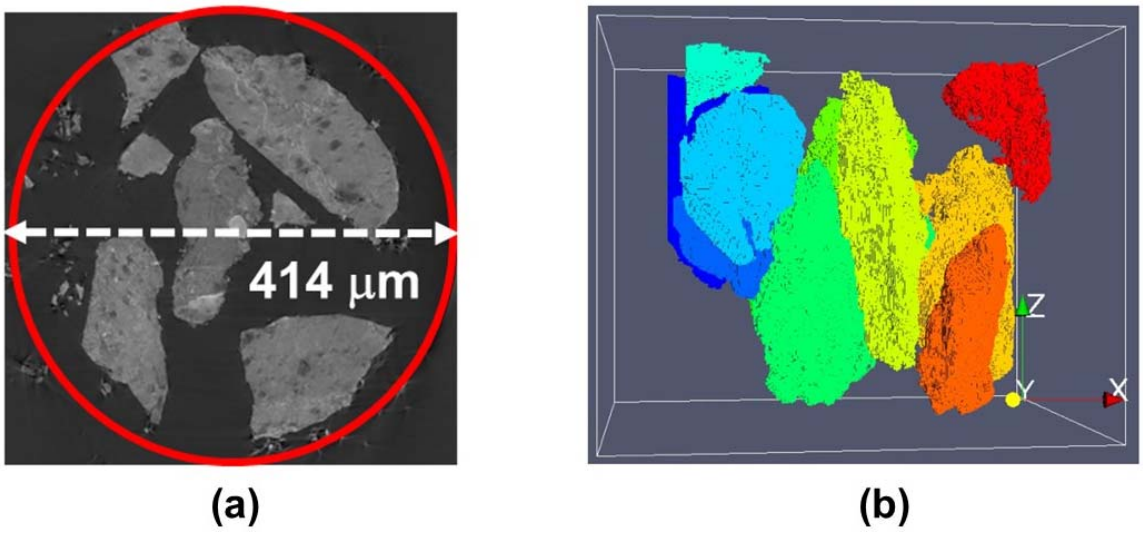


**Fig. 17.** (a) 2D slice of the raw XTM images made from a sample of many particles placed in a circular tube of 414 μm in diameter. (b) The collection of eleven 3D reconstructed porous catalytic particles made after segmentation of the raw images.

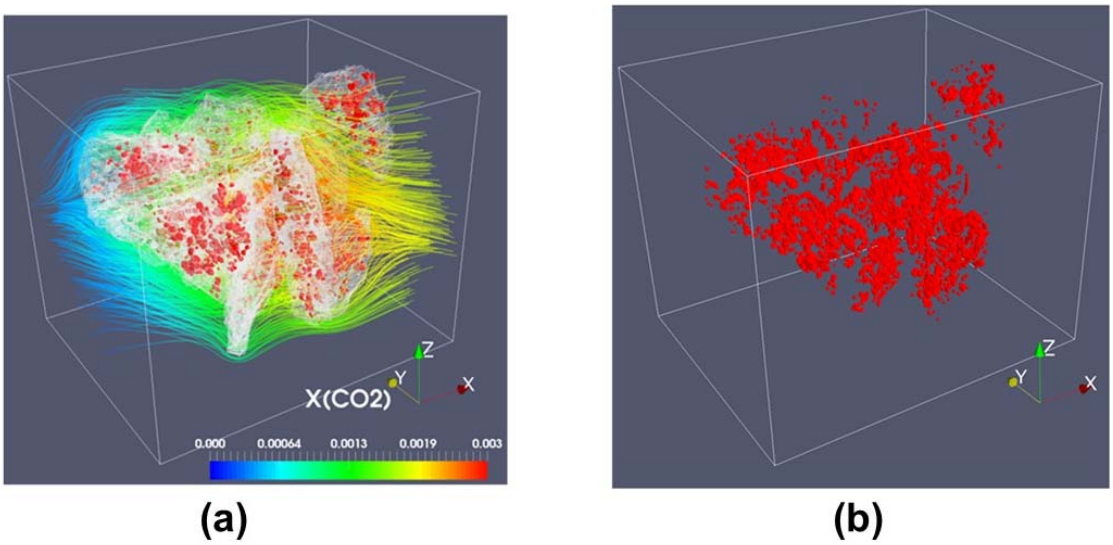


**Fig. 18.** (a) Flow streamlines colored in concentration of $CO_2$ over eleven static catalytic particles. (b) Visualization of the pore-spaces containing high concentration of $CO_2$ for all particles.

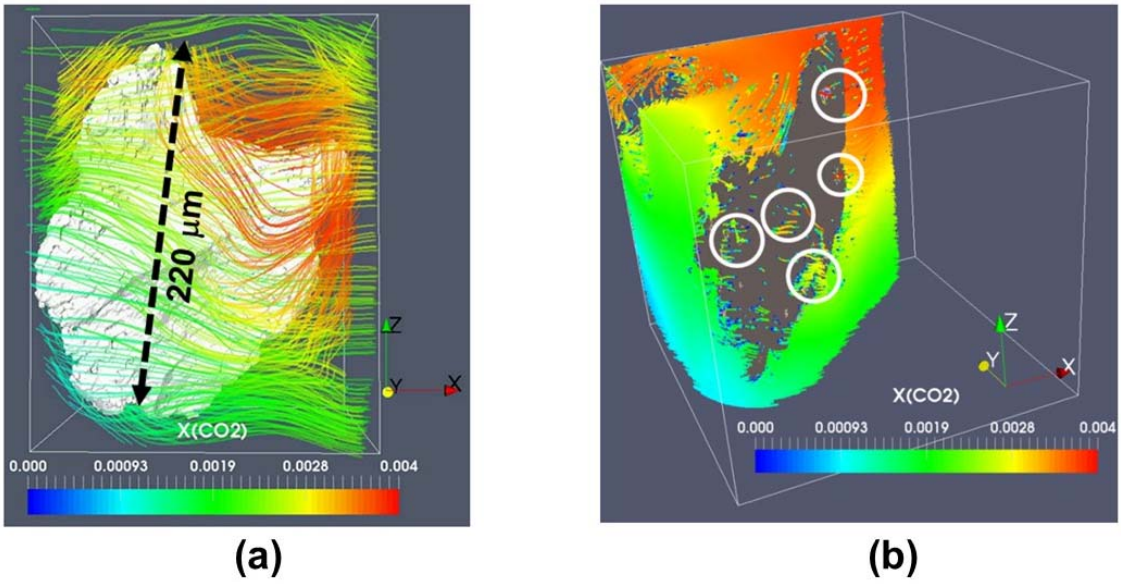


**Fig. 19.** (a) Flow streamlines around a single porous catalytic particle obtained from XTM, (b) cut-view of the same particle to probe the streamlines inside the particle pores.

To this end, a sample of a group of particles used in the methanation experiments at PSI were provided to PSI's TOMCAT beamline facility, to obtain high resolution phase-contrasted XTM images of the 3D porous map of the real particles. The sample was made in the form of a circular tube of 414 μm in dimeter, containing a number of particles. Eventually 3D XTM data were collected for a group of 11 particles of different size and shapes, with the help of Dr. Anne Bonnin (SLS scientist). The obtained images had a voxel size of 0.162 μm taken at an optical zoom of 40X (corresponding to a maximum numerical resolution of 2x0.162 μm = 0.324 μm). A 2D slice of the raw gray-scale images is depicted in Fig. 17(a), which was subsequently converted by our group into segmented binary

images and reconstructed to obtain the full 3D structure of the particles used in the numerical solver as shown in Fig. 17(b). The final binary data as used in the numerical solver is binned to have 1 μm resolution, which preserves the porous structure to a great degree but reduces the memory size considerably and fits the data into existing computational resources.

Upon preparing the sample to be used in the simulations, preliminary simulations for the benchmark reaction of methane and oxygen were performed using the static group of the 11 particles to investigate the extent of intra-particle contribution onto the overall reaction performance. As shown in Fig. 18, the simulation consisted of a cubic domain 0.5 mm in each direction. The flow streamlines colored in $CO_2$ concentration were visualized for the entire domain in Fig. 18(a), while a 3D rendering of those pore spaces, which actively participated in the reaction and diffusion, is presented in Fig. 18(b). The latter results showed that the total volume of such active pores amounted to ~15% of the total solid volume of the particles, which confirmed the importance of the intra-particle diffusion. Moreover, a closer observation of the flow and diffusion inside the individual particles could be obtained via a cut-view of a single porous particle; therein, the flow streamlines and the concentration distribution inside the porous network were monitored as illustrated in Fig. 19. The white circles marked in Fig. 19(b) indicated those channels deep inside the particle that contained high concentration of product and yet experienced a low flow velocity that promoted transport towards the rest of the gaseous mixture inside and outside the particle.

## 4.4 High performance computing

The inclusion of several gas species into the flow solver and the flow tracking on large domain sizes and over long convergence times, as required in the present simulations, led to demanding computational loads in terms of run time and memory. Therefore, implementations based on legacy serial or single PC-based multi-core protocols precluded capturing the full picture of the desired phenomena. Thanks to the highly scalable algorithm of the LB method, we designed our 3D multicomponent package based on parallel implementation on multiple general purpose graphics processing units (GPGPUS) which was run on large GPGPU clusters such as those at CSCS Mano. The implementation was thus pursued in a hybrid CUDA-MPI discipline, combining multiple-core GPU programming with message passing techniques for physically separate, distributed memory computer nodes.


**Fig. 20.** (a) The local compute cluster of Dr. Mantzaras' group at PSI consisting of 4 Nvidia's Tesla K80 GPGPUs. (b) the Piz-Daint GPGPU cluster of the Swiss Supercomputing Center used for the long production runs

Currently, we run the simulations on an in-house cluster of 4 K80 GPGPUs depicted in Fig. 20, which can deliver converged solutions within less than 24 hours. This enables multiple successive jobs in short times, optimizes the free physical parameters, and reaches a final solution within reasonable times and costs.

During the second project year, significant improvement of the GPU code performance was attained by the parallel calculation of the aerodynamic forces exerted on a moving particle. In this latest development, data was not copied from GPU to CPU for integration/reduction, thus leading to a significant 25% increase in the overall performance.

# 5 Discussion of results

## 5.1 Development of numerical code

The newly developed numerical code has shown very good scalability in multiple GPUs and has implemented a wealth of new physical models. The developed tool was the first LB code capable of simulating a moving particle with catalytic reactions in its internal and external surfaces. Such an inclusion of aerodynamic forces exerted on the particle, catalytic chemical reactions and proper interfacial gas/solid boundary conditions for complex geometries had not been attempted in the past.

## 5.2 Particle characterization

The capacity of the phase-contrasted X-ray tomography (XTM) at the TOMCAT beamline of SLS in providing very high quality geometric reconstructions of porous particles, with very good discrimination between void and solid, was firmly demonstrated. Multiple catalytic particles were scanned and 3D reconstructed images of the particles' external surface as well as the internal porous structures were obtained with a spatial resolution of ~0.16 μm. This finding paves the way for more detailed future investigation (interrogation of different particle sizes) of particle geometries.

## 5.3 Physics extracted from first simulations

First reactive flow simulations were performed, not for the biogas methanation catalytic reactions but for the catalytic total oxidation of methane. This reaction platform was easier for code benchmarking, but still yielded a wealth of new physical insights:

- Simulations revealed the contribution of the particle's internal porosity to the overall reaction performance. Considering first a stationary particle, reactants were supplied via convective transport in the upstream front of the particle, whereas diffusive transport acted to equalize the species distribution inside the particle such that complete reaction could occur due to the increased residence time of the mixture. In the absence of large velocities inside the particle, diffusion carried the burnt gases towards the low velocity wake behind the particle.
- Of prime importance for the investigation of the biogas methanation process was the simulation of a moving particle. Such simulations showed that gases, which were rich in product species and were trapped inside the particles, were convected with the particle as it moved along the streamwise direction. Compared to the stationary particle simulation, in the moving particle simulation the product distribution extended over a larger area in front of the particle, exhibiting a stronger diffusive process in the upstream direction, since now diffusion was strong enough to compete with the reduced velocity (convection) of the flow relative to the moving particle. This finding gave credence to the hypothesis that the trapped gases inside

catalytic particles of methanation fluidized beds were responsible for an increased axial dispersion that needed to be accounted for in macroscopic FB models.

- Simulations on real particle geometries extracted from phase-contrasted XTM indicated that the even real particles with very low porosities could absorb and carry substantial amount of gas over time, which was contributing to the overall reaction rate of the system.

# 6 Conclusions and outlook

A new LB reacting flow code has been contructed for the modeling of moving and reacting porous cataytic particles. Key model features are the following:

- New catalytic boundary conditions (interfacial solid/gas) were developed for irregular catalytic surfaces in 3D.
- Simulations on stationary porous solid object with different pore sizes and isothermal conditions were conducted. The code, as it stands, is ready to be used for simulation of catalytically reacting particles not only in methanation in FBs but also in FBs used for granulation, polyethylene production and fluid catalytic cracking (FCC).
- The solver was extended by including a moving particle under a prescribed velocity, into the new catalytic boundary conditions. Special attention was paid to avoid jump of the hydrodynamic properties and species concentrations as the boundary moves and leaves new fluid regions behind. Rigorous check for global mass and momentum conservation of species as well as individual elements for a 3D porous moving particle was performed.

Initial X-ray phase-contrasted tomography measurements of the methanation Ni-$Al_2O_3$ particles were carried out at the Swiss Light Source (SLS) TOMCAT beamline od PSI, in order to assess the true porous geometry. The capacity of the technique to provide high-reolution images (~0.3 $\mu$m) with very good discrimination between solid and internal void structure (porous network) has been demonstrated. This constitutes the first time where phase-contrasted XTM (a technique developed at PSI) has been successfully applied to reconstruct with sub-micron resolution the internal porous structure of particles. This paves the way for applications to other energy conversion systems, such as diesel partcle filters (DPF) and washcoated catalysts in fuel processing systems.

Initial simulations were carried out under stationary and moving conditions for the total catalytic oxydation of methane on the group of real particles obtained from XTM. These simulations confirmed the role of the trapped gases (inside the particle porous network) on the overall reaction performance. Such findings are also of interest to modeling of other energy conversion systems, such as particles in DPFs, coombusiton of coal and wood particles, etc.

Contrary to the limited experimental conditions and data, the numerical tool has provided an exceptional chance to artificially change various parameters of the simulation, e.g. porosity, reaction rate, initial concentrations, catalyst coating coverage, etc. so as to collect a large sensitivity analysis data base to be used in future FB design improvements.

## 6.1 Next steps after end of project

In order to accomplish the goals of the full three-year project, the following steps are required. These steps involve the work of a new PhD student who just started (January 2019) working on the single catalytic particle (SCP) case. Provided that funding is also granted for a postdoc (proposal submitted

to the PSI-FELLOW program, with a decision pending in March 2019) the multiple catalytic particles (MCP) case will also be investigated.

**1)** Evaluate the effect of the catalytic reactions exothermicity on the temperature distribution inside the particles using a finite difference solver for the heat conduction inside the solid phase which will be coupled with the LB solver via heat convection at the surface. Expected delivery September 2019.

**2)** Enhance the solver to include thermal effects in the gas phase based on the method already developed in our group [41] and verify whether the temperature gradients inside the gas phase are significant in the vicinity of the moving particle. Expected delivery January 2020.

**3)** Perform additional XTM measurements at the TOMCAT beamline of SLS to characterize the internal pore networks of catalytic particles having different sizes.A new proposal to SLS will be submitted in March 15, 2019 to secure beamtime (3 shifts) for experiments in the fall of 2019.

**4)** Enhance the current state of the hydrodynamic force calculations to include the angular moments needed to update the orientation of the particle as a real non-spherical particle is rotated by the flow inside the FB. Expected delivery November 2019.

**5)** Introduce the principal methanation reactions and use original XTM-based geometries of different particle samples; perform sensitivity analysis for the global reaction performance over a wide range of porosity, reaction kinetics, operating temperature, particle velocity, and inlet conditions. Expected delivery June 2020.

**6)** Start the MCP problem for non-porous particles; develop a computationally efficient algorithm to solve for the movement and interactions of multiple non-porous particles based on the soft-collision method and couple it with flow and reaction. Expected delivery September 2020.

**7)** To include the effect of internal porosity into the MCP problem, various upscaling strategies for homogenization of a single porous particle (particle training) will be tested. Fine tuning of the upscaling process will be done by extensive comparisons between the fully resolved and up-scaled simulations. Expected delivery January 2011

**8)** Augment the existing macroscopic FB models at PSI, in light of the microscopic simulation results. The current two-phase (bubble (gas) and emulsion (solid)) 1D macroscopic model will be extended to include three phases: phase bubble (gas), emulsion (solid), and intra-particle trapped gas. Expected delivery March 2020.

# 7 Publications [within the project]

The newly developed model for catalytic reacting boundary conditions at complex (irregular 3D geometries) gas-solid interfaces was applied, for the first time, not in the field of biogas methanation, but in porous gas diffusion layers of polymer electrolyte fuel cells. The mathematical model used by our group in the following publication is the model developed in this BfE project.

PSI_2019 M.A. Safi, J. Mantzaras, N.I. Prasianakis, A. Lamibrac, F.N. Büchi, "A pore-level direct numerical investigation of water evaporation characteristics under air and hydrogen in the gas diffusion layers of polymer electrolyte fuel cells", International Journal of Heat and Mass Transfer 129 (2019) 1250-1262.
https://doi.org/10.1016/j.ijheatmasstransfer.2018.10.042

# 8 References


[1] M.P. Martin, P. Turlier, R. Bernard, G. Wild, Powder Technol. 70 (1992) 249-258.

[2] G. Jimenez-Garcia, R. Aguilar-Lopez, R. Maya-Yescas, Fuel 90 (2011) 3531-3541.

[3] E.W. Lang, H.G. Smith, Ind. Eng. Chem. 49 (1957) 355-359.

[4] J. Van Caneghem, A. Brems, P. Lievens, C. Block, P. Billen, I. Vermeulen, R. Dewil, J. Baeyens,.C. Vandecasteele, Prog. Energy Combust. Sci. 38 (2012) 551-582.

[5] M.C. Seemann, T.J. Schildhauer, S.M.A. Biollaz, Ind. Eng. Chem. Res. 49 (2010) 7034-7038.

[6] J. Kopyscinski, T.J. Schildhauer, S.M.A. Biollaz, Ind. Eng. Chem. Res. 50 (2011) 2781-2790.

[7] M. Ruedisueli, T.J. Schildhauer, S.M.A. Biollaz, J.R. van Ommen, Ind. Eng. Chem. Res. 51 (2012) 4748-4758.

[8] J. Kopyscinski, T.J. Schildhauer, S.M.A. Biollaz, Chem. Eng. Sci. 66 (2011) 924-934.

[9] V. Verma, T.W. Li, J.F. Dietiker, W.A. Rogers, Chem. Eng. J. 287 (2016) 727-743.

[10] M. Ruedisueli, T.J. Schildhauer, S.M.A. Biollaz, J.R. van Ommen, Ind. Eng. Chem. Res. 51 (2012) 4748-4758.

[11] C.R. Mueller, G. Hartung, J. Hult, J.S. Dennis, C.F. Kaminski, AIChE J. 55 (2009) 1369-1382.

[12] D.J. Holland, C.R. Mueller, A.J. Sederman, M.D. Mantle, L.F. Gladden, J.F. Davidson, Theor. Found. Chem. Eng. 42 (2008) 469-478.

[13] K.A. Buist, T.W. van Erdewijk, N.G. Deen, J.A.M. Kuipers, AIChE J. 61 (2015) 3198-3207.

[14] D. Geldart, Powder Technol. 7 (1973) 285-292.

[15] M.A. van der Hoef, M.V. Annaland, N.G. Deen, J.A.M. Kuipers, in: Ann. Rev. Fluid Mech., Annual Reviews, Palo Alto, 2008, pp. 47-70.

[16] T.B. Anderson, R. Jackson, Ind. Eng. Chem. Fundam. 8 (1969) 137-144.

[17] J.A.M. Kuipers, K.J. Vanduin, F.P.H. Vanbeckum, W.P.M. Vanswaaij, Chem. Eng. Sci. 47 (1992) 1913-1924.

[18] S. Ergun, Chem. Eng. Prog. 48 (1952) 89-94.

[19] C.Y. Wen, Y.H. Yu, Chem. Eng. Prog. Symp. Ser. 62 (1966) 100-111.

[20] U. Lacis, K. Taira, S. Bagheri, J. Comput. Phys. 305 (2016) 300-318.

[21] M.V. Papalexandris, P.D. Antoniadis, Int. J. Heat Mass Transf. 88 (2015) 42-54.

[22] B.P.B. Hoomans, J.A.M. Kuipers, W.J. Briels, W.P.M. van Swaaij, Chem. Eng. Sci. 51 (1996) 99-118.

[23] G.A. Bokkers, J.A. Laverman, M.V. Annaland, J.A.M. Kuipers, Chem. Eng. Sci. 61 (2006) 5590-5602.

[24] Y.R. He, T.Y. Wang, N. Deen, M.V. Annaland, H. Kuipers, D.S. Wen, Particuology 10 (2012) 428-437.

[25] A.J.C. Ladd, J. Fluid Mech. 271 (1994) 285-309.

[26] U. Lacis, K. Taira, S. Bagheri, J. Comput. Phys. 305 (2016) 300-318.

[27] M. Uhlmann, J. Comput. Phys. 209 (2005) 448-476.

[28] Y. Tang, E. Peters, J.A.M. Kuipers, S.H.L. Kriebitzsch, M.A. van der Hoef, AIChE J. 61 (2015) 688-698.

[29] M.A. Van der Hoef, R. Beetstra, J.A.M. Kuipers, J. Fluid. Mech. 528 (2005) 233-254.

[30] J. Kopyscinski, T.J. Schildhauer, S.M.A. Biollaz, Chem. Eng. Sci. 66 (2011) 1612-1621.

[31] Y.F. Liu, O. Hinrichsen, Ind. Eng. Chem. Res. 53 (2014) 9348-9356.

[32] J. Kopyscinski, T.J. Schildhauer, F. Vogel, S.M.A. Biollaz, A. Wokaun, J. Catal. 271 (2010) 262-279.

[33] J. Solsvik, H.A. Jakobsen, Chem. Eng. Sci. 66 (2011) 1986-2000.

[34] J. Solsvik, H.A. Jakobsen, , Chem. Eng. J. 178 (2011) 407-422.

[35] A. Guardo, M. Casanovas, E. Ramírez, F. Recasens, I. Magaña, D. Martínez, M.A. Larrayoz, Chem. Eng. Sci. 62 (2007) 5054-5061.

[36] D. Kunii, O. Levenspiel, Fluidization Engineering, Wiley, New York, 1968.

[37] N. Mostoufi, J. Chaouki, Chem. Eng. Res. Des. 78 (2000) 911-920.

[38] J.F. Davidson, D. Harrison, Fluidized Particles, Cambridge University Press, New York, 1963.

[39] S. Arcidiacono, J. Mantzaras, I.V. Karlin, C.E. Frouzakes, Phys. Rev. E 76 (2007) 046703.

[40] S. Arcidiacono, J. Mantzaras, I.V. Karlin, Phys. Rev. E 78 (2008) 046711.

[41] J.F. Kang, N.I. Prasianakis, J. Mantzaras, Phys. Rev. E 89 (2014) 063310.

[42] M.A. Safi, M. Ashrafizaadeh, Int. J. Comput. Sci. Eng. 12 (2016) 298-310.

[43] A.J.C. Ladd, J. Fluid. Mech. 271 (1994) 311-339.

[44] N.I. Prasianakis, T. Rosen, J. Kang, J. Eller, J. Mantzaras, F.N. Buchi, Commun. Comput. Phys. 13 (2013) 851-866.

[45] Z. Yu, L.-S. Fan, J. Comput. Phys. 228 (2009) 6456-6478.

[46] J.M. Blasi, P.J. Weddle, C. Karakaya, D.R. Diercks, R.J. Kee, Chem. Eng. Sci. 145 (2016) 308-316.

[47] M.A. Safi, N.I. Prasianakis, J. Mantzaras, A. Lamibrac, F.N. Büchi, Int. J. Heat Mass Trans. 115 (2017) 238-249.

[48] M.A. Safi, J. Mantzaras, N.I. Prasianakis, A. Lamibrac, F.N. Büchi, Int. J. Heat Mass Trans. 129 (2019) 1250-1262.

[49] M. Reinke, J. Mantzaras, R. Schaeren, R. Bombach, A. Inauen, S. Schenker, Combust. Flame 136 (2004) 217-240.